



Quantile-based sequential optimization and reliability assessment for shape and topology optimization of plane frames using L-moments

Wei Shen^{a,*}, Makoto Ohsaki^a, Makoto Yamakawa^b

^a Department of Architecture and Architectural Engineering, Graduate School of Engineering, Kyoto University Kyoto-Daigaku Katsura, Nishikyo, Kyoto 615-8540, Japan

^b Department of Architecture, Tokyo University of Science, 6-3-1 Niijuku, Katsushika-ku, Tokyo 125-8585, Japan

ARTICLE INFO

Keywords:

Quantile function
Sample L-moment
Sequential optimization and reliability assessment
Shape and topology optimization
Force density method
Maximum entropy method

ABSTRACT

Uncertainty is inevitable in the real physical world, and it is necessary to take into account its effects on the structural design and optimization processes. In this study a reliability-based shape and topology optimization method is proposed for plane frames. The reliability constraint is expressed in terms of quantile which is estimated by using the maximum entropy method subject to constraints on the sample linear moments (L-moments) with small sample size. An iterative scheme of sequential optimization and reliability assessment is employed to solve a series of deterministic optimization problems with shifted boundaries on the constraints. Derivative of the quantile function is obtained by solving a convex optimization problem, instead of solving a system of nonlinear equations. Force density method is applied to an auxiliary truss model for simultaneous shape and topology optimization of plane frames to alleviate the difficulties caused by melting nodes. It is demonstrated by the benchmark and numerical examples that the quantile function can be appropriately estimated by the proposed method, and the solution satisfying the required reliability constraint can also be achieved.

1. Introduction

Due to the uncertain nature of the real world engineering design problems, it has been well recognized that structural optimization which takes uncertainties into consideration receives more and more attention and plays an important role in practical engineering [1–3]. Among them, one of the popular methods to incorporate uncertainty in an optimization problem is reliability-based design optimization (RBDO) which focuses on finding the best solution satisfying the target reliability constraints [4,5]. In this section the definitions of RBDO problem and some technical terms related to the problem are briefly given at first, and then the existing researches on solving the problem are discussed.

1.1. Problem definition

Let $\mathbf{d} = (d_1, d_2, \dots, d_{n_d})$ and $\boldsymbol{\theta} = (\theta_1, \theta_2, \dots, \theta_{n_\theta})$ denote the vectors of n_d design variables and n_θ random variables with the specified distribution, respectively. The RBDO problem can be generally given as [5]

$$\begin{aligned} & \text{Minimize } W(\mathbf{d}) \\ & \text{subject to } \Pr \left\{ g_j(\mathbf{d}; \boldsymbol{\theta}) \leq \bar{g}_j \right\} \geq R_j, \quad j = 1, 2, \dots, n; \quad \underline{\mathbf{d}} \leq \mathbf{d} \leq \bar{\mathbf{d}} \end{aligned} \quad (1)$$

where $W(\mathbf{d})$ is the objective function to be minimized; $g_j(\mathbf{d}; \boldsymbol{\theta})$ is the j th performance function under uncertainty and n is the number of performance functions; \bar{g}_j is the prescribed upper bound of $g_j(\mathbf{d}; \boldsymbol{\theta})$ and R_j is the target probability of $g_j(\mathbf{d}; \boldsymbol{\theta})$ not to exceed \bar{g}_j ; $\underline{\mathbf{d}}$ and $\bar{\mathbf{d}}$ are the vectors of lower and upper bounds for \mathbf{d} , respectively. Note that the vector of design variables \mathbf{d} in problem (1) includes deterministic design variables and the mean values of random design variables.

According to Refs. [6,7], the approaches for solving problem (1) can be classified into the following three categories in view of their strategies to incorporate probabilistic constraints in optimization procedure, and their corresponding schematic presentations are shown in Fig. 1:

(1) Double-loop method directly solves problem (1) in which the probability constraints are evaluated at each iteration of the optimization procedure with the current values of design variables. Therefore, there are two nested cycles in the double-loop method: the inner cycle evaluates the probability constraints at each iteration of the outer cycle of optimization procedure.

(2) Single-loop method: the single-loop method avoids the inner cycle in double-loop method by converting probability constraints into approximated deterministic constraints at the most probable point (MPP) [8]. In this way, it allows to avoid the inner cycle and reduces the

* Corresponding author.

E-mail addresses: shen.wei.28a@st.kyoto-u.ac.jp (W. Shen), ohsaki@archi.kyoto-u.ac.jp (M. Ohsaki), myamakawa@rs.tus.ac.jp (M. Yamakawa).

computational cost. Another construction of single-loop method is to use the Karush-Kuhn-Tucker optimality conditions of the inner problem to convert the RBDO problem to a deterministic optimization problem [9,10].

(3) Decouple method: The decoupling method asymptotically solves problem (1) by a series of sub-deterministic optimization problems. The information from the reliability analysis is extracted and used to construct the sub-deterministic optimization problems such that it is not necessary to implement a full reliability analysis each time when a new point of design variables is found by the optimization procedure.

1.2. Literature review

Although the double-loop method is easy to implement, it would become computationally infeasible because it consists of nested loops of design optimization and reliability analysis [11]. Therefore, great effort has been made in the past two decades to improve its efficiency by either facilitating the procedure of reliability analysis [12] or modifying the formulation of probability constraints [13]. Lee *et al.* [14] introduced the popular dimensional reduction method (DRM) into the double-loop RBDO with a new inverse reliability analysis to reduce the number of function evaluations in multidimensional probability integration; Rahman and Wei [15] also applied DRM to double-loop RBDO procedure where the sensitivity coefficients of probability with respect to design variables are derived. However, since the inner loop of reliability analysis is called at each time when the design variables are updated at the outer loop, the number of reliability analyses could be still very large which may lead to a high computational cost. On the other hand, single-loop method provides an alternative to reduce the number of RBDO function calls. Chen *et al.* [8] firstly proposed the single-loop single vector method where the unit direction vector for searching MPP is assumed to be constant, and Liang *et al.* [10] further developed the method by adaptively calculating the unit direction vector during the optimization procedure. It is proven that the single-loop method is one of the most efficient approaches for solving RBDO problems [16], but its numerical stability is still a challenge when the limit state function is highly nonlinear [7].

The decoupling method improves the efficiency of double-loop

method from another perspective where the inner cycle of reliability analysis is decoupled from the outer cycle of optimization and the evaluation of probabilistic constraints only need to be conducted at the end of each sub-deterministic optimization process. Early work of decoupling method approximates the probability constraint using sensitivity information of the previous iteration [17]. Du and Chen [18] proposed the sequential optimization and reliability assessment (SORA) method which decouples the reliability analysis from structural optimization using the shifting vector. Since then, SORA has gradually become one of the frequently used methods for solving RBDO problems because of its simplicity and stability [7], and many researches have been conducted to enhance its performance. Du [19] further improved the accuracy of SORA by using saddle point approximation to handle the nonlinearity in probability constraints caused by the transformation between non-normal and normal random variables. Chen *et al.* [20] searched the optimal shifting vector using the limit state functions to accurately adjust the boundaries of probability constraints when they are highly nonlinear. However, as most of the existing SORAs are MPP-based methods, one of the challenges is that the MPP-based SORA may not be able to converge if there are multiple MPPs [21]. To overcome this difficulty, recently Li *et al.* [22] proposed a quantile-based SORA method where the shifting vector is calculated in the probability space without relying on the MPP. The Kriging model is also applied instead of the crude Monte Carlo simulation (MCS) to reduce the computational cost for calculating the quantile. He *et al.* [23] further extended the quantile-based SORA method by calculating the quantile corresponding to the target reliability using fractional moment-based maximum entropy method (MEM), and the two-level optimization problem to obtain the values of Lagrangian multipliers and the orders of fractional moments is reduced to a single-loop optimization problem by using Laplace transform [24]. However, the Laplace transform of unknown probability distribution function (PDF) needs to be carefully chosen otherwise it may spoil the result [24]. Do *et al.* calculate the desired quantile by using inverse saddlepoint approximation where the mixture of Gaussian process is exploited for modeling the performance function under uncertainty [25].

While the general framework of quantile-based SORA explores the possibility of using MPP-free reliability analysis methods, another

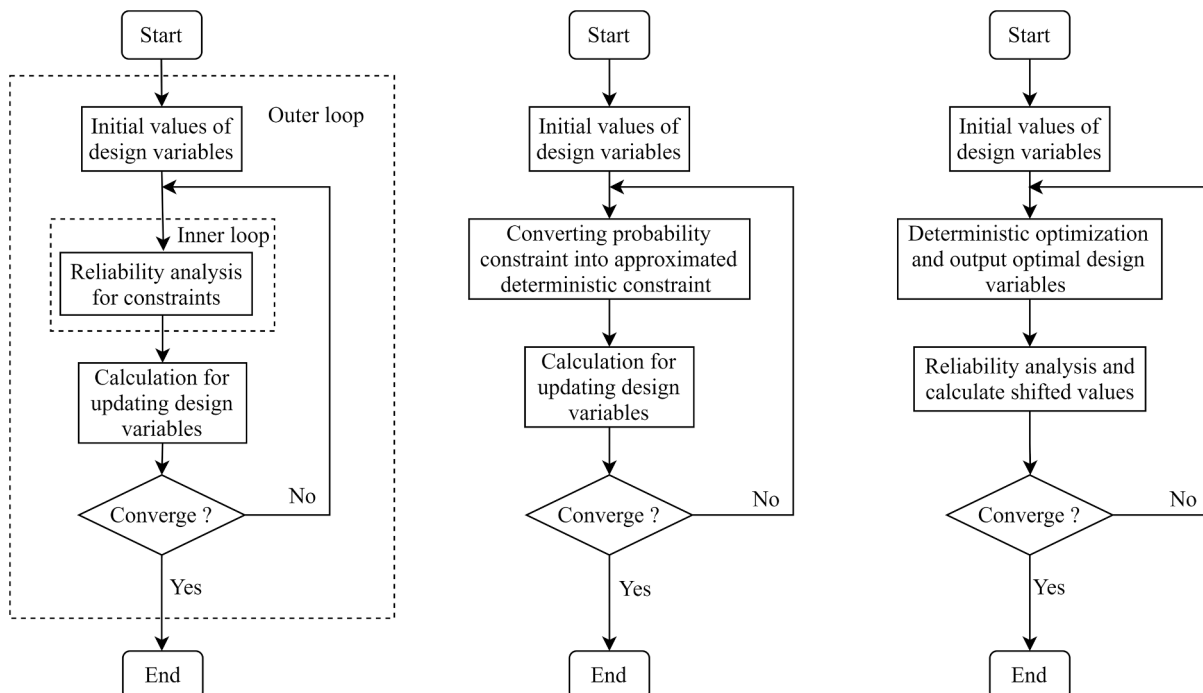


Fig. 1. Strategies for solving RBDO problem, from left to right: double-loop method, single-loop method and decouple method.

challenge is that in practice the exact probability information of uncertainty may be unavailable beforehand and one would need to calculate the structural reliability with a given set of random samples [26,27]. Moreover, the sample size and sampling variability have great effect on the accuracy of surrogate model used for structural simulation and the sample central moments used for probability estimation [28–31]. To overcome such difficulties, Pandey [32] estimated the quantile function of a non-negative random variable with unknown distribution using MEM subject to sample probability-weighted moments (PWM) obtained from random samples, and the results showed that this method is more reliable than the method using sample central moments when sample size is small. Deng and Pandey [33] further improved this method with fractional PWM, but the Lagrange multipliers and the orders of fractional moments are determined by the two-level nested optimization procedure which is computationally expensive. Besides, since the single-level method in Ref. [24] is constructed for ordinary fractional moments, it cannot be directly applied to quantile-based MEM subject to fractional PWM constraints. On the other hand, Pandey [34,35] also presented an approach for quantile estimation of a non-negative random variable by using minimum cross-entropy principle (MCEP) subject to PWM constraints, and stated that if the prior distribution in MCEP is uniform, the cross-entropy minimization is equivalent to entropy maximization. However, since MCEP requires a prior distribution for quantile estimation, the MEM is more appropriate than MSEP when any prior information is absent. Hosking [36] found that the maximum entropy distribution of an unknown random variable having specified linear moments (L-moments) has a density-quantile function in a polynomial form which is the derivative of the quantile function, and the quantile function can then be obtained by numerical integration, whereas the unknown coefficients in density-quantile function are derived by solving a system of nonlinear equations.

Optimization of truss-like structures is one of the well investigated fields in structural optimization; see the review articles [37,38] and text books [39,40] for a comprehensive summary. However, there still remains some difficulties for simultaneous optimization of shape and topology optimization, and extensive and valuable contributions have been made in the past decades to the development of mathematical formulations and optimization methods. Although the ground structure method is widely used to find the optimal topology of the truss-like structures [41,42], it is necessary to work with as many nodes and members as possible because the nodal locations are unable to vary during the optimization process. On the other hand, since the adjustment of nodal locations can usually lead to effective improvement of objective function value [43,44], one can start from a sparse ground structure if the shape optimization is involved. However, when the nodes are allowed to move in a wide range of the design space, one of the main difficulties is the existence of melting nodes or coalescent nodes which results in extremely short members in the structure and makes the stiffness matrix singular [45,46]. To alleviate the problem caused by melting nodes, Ohsaki and Hayashi [47,48] explored the merit of force density method (FDM) to shape and topology optimization of pin-jointed trusses, in which the objective and constraint functions are expressed explicitly by force density only, and Shen and Ohsaki [49] extended the method to the optimization of rigidly-jointed frames.

In this paper, we proposed a quantile-based SORA method for simultaneous shape and topology optimization of plane frames under reliability constraints. The uncertainties are assumed to exist in the nodal locations and the cross-sectional area and Young's modulus of each member. The reliability constraint is expressed in terms of quantile which is estimated using MEM subject to the constraints on sample L-moments. Compared with Refs. [22,23], the main difference of the proposed method is that no assumptions on the distributions of uncertainties are made and the samples can be obtained by any randomization method without specifying the probability distribution. Besides, in order to avoid the extremely short members during shape optimization [45,47,48], the shape of frame structure is determined by a set of

force densities of the auxiliary truss that is irrelevant to the true loading and boundary conditions of the frame to be optimized [49].

The rest of the paper is organized as follows. In Section 2 the concept of quantile-based SORA is briefly introduced, and the estimation of quantile function using MEM subject to the constraints on sample L-moments is given in Section 3. Section 4 presents the problem formulation of shape and topology optimization of a plane frame under uncertainty, which is mainly based on the framework discussed in Section 2. One benchmark example and four numerical examples are investigated in Section 5 to demonstrate the accuracy and effectiveness of the proposed method. Finally, some conclusions are drawn in Section 6.

2. Quantile-based SORA

In this section, the basic concept of quantile-based SORA is briefly introduced [22,23]. The main difference of the quantile-based SORA from traditional SORA is that the shifting vector is calculated using quantile instead of the MPP. Based on Eq. (1) and the equivalent description between the reliability constraint and the quantile of structural response [50], we define the following n quantiles

$$Q_{R_j}(\mathbf{d}; \boldsymbol{\theta}) = \inf \{ Q : \Pr \{ g_j(\mathbf{d}; \boldsymbol{\theta}) \leq Q \} \geq R_j \}, j = 1, 2, \dots, n \quad (2)$$

as alternatives for the n reliability constraints in problem (1), where $Q_{R_j}(\mathbf{d}; \boldsymbol{\theta})$ is the j th quantile corresponding to the j th performance function $g_j(\mathbf{d}; \boldsymbol{\theta})$ and target probability R_j . Then, we can rewrite the problem (1) in terms of quantile as follows:

$$\begin{aligned} &\text{Minimize } W(\mathbf{d}) \\ &\text{subject to } Q_{R_j}(\mathbf{d}; \boldsymbol{\theta}) \leq \bar{g}_j, j = 1, 2, \dots, n; \quad \underline{\mathbf{d}} \leq \mathbf{d} \leq \bar{\mathbf{d}} \end{aligned} \quad (3)$$

It can be observed that the target values of probability R_j ($j = 1, 2, \dots, n$) are now implicitly incorporated in problem (3) by the corresponding quantiles defined in Eq. (2), bridging the equivalence between problems (1) and (3) [50]. The random variables in problem (3) are assumed to be mutually independent. For general cases where some or all the random variables are correlated, they can be transformed into independent random variables by various methods like the well-known Rosenblatt or Nataf transformations [51,52] or other transformation methods without requiring the marginal PDF of each random variable [53]. Therefore, for simplicity in this study the discussion of reliability-based optimization problem is limited to independent random variables.

According to the quantile-based SORA [22,23], the optimal solution of problem (3) can be obtained by solving a series of deterministic optimization problems where the upper bounds for performance functions are shifted at each iteration to ensure that the quantile $Q_{R_j}(\mathbf{d}; \boldsymbol{\theta})$ is on the boundary. Denote the shifting value of \bar{g}_j at the $(k + 1)$ th iteration as \bar{c}_j^{k+1} , the $(k + 1)$ th deterministic optimization problem of quantile-based SORA is then formulated as

$$\begin{aligned} &\text{Minimize } W(\mathbf{d}) \\ &\text{subject to } g_j(\mathbf{d}) \leq \bar{c}_j^{k+1}, j = 1, 2, \dots, n; \quad \underline{\mathbf{d}} \leq \mathbf{d} \leq \bar{\mathbf{d}} \end{aligned} \quad (4)$$

and \bar{c}_j^{k+1} is calculated by

$$\bar{c}_j^{k+1} = Q_{R_j}(\mathbf{d}^k; \boldsymbol{\theta}) - g_j(\mathbf{d}^k), j = 1, 2, \dots, n \quad (5)$$

where \mathbf{d}^k is the solution of problem (4) at the k th iteration and $g_j(\mathbf{d}^k)$ is the value of j th performance function without uncertainty; $Q_{R_j}(\mathbf{d}^k; \boldsymbol{\theta})$ represents the quantile corresponding to the solution \mathbf{d}^k . Because the solution of problem (4) has not been found yet at the initial iteration (i. e., $k = 0$) and there is no information about the corresponding quantile, the value of \bar{c}_j^1 is set to 0 for the initial iteration [18].

Equations (4) and (5) constitute one iteration of quantile-based SORA, and in order to prevent obtaining a conservative result, the optimization procedure is considered convergent at the k th iteration if

all the reliability constraints are satisfied and at least one of them retain equality, namely:

$$\begin{aligned} Q_{R_j}(d^k; \theta) &\leq \bar{g}_j, j = 1, 2, \dots, n \text{ and} \\ Q_{R_{j_e}}(d^k; \theta) &= \bar{g}_{j_e}, \exists j_e \in \{1, 2, \dots, n\} \end{aligned} \quad (6)$$

3. Estimation of quantile

As discussed in Section 2, one of the main steps in quantile-based SORA is to calculate the quantile $Q_{R_j}(d^k; \theta)$ in Eq. (5) after solving problem (4) at each iteration. In this section a quantile estimation method is proposed for obtaining the desired quantile $Q_{R_j}(d^k; \theta)$, which utilizes the MEM subject to constraints specified in terms of sample L-moments [29,31].

Suppose after the k th iteration the j th ($j = 1, 2, \dots, n$) performance function under uncertainty is a continuous random variable $Z_j^k = g_j(d^k; \theta)$ with cumulative distribution function (CDF) $F_j^k(z_j^k)$ and PDF $f_j^k(z_j^k)$. Let $Q_j^k(q)$ and $Q_j^{k'}(q)$ denote the quantile function of Z_j^k and its corresponding derivative for $0 < q < 1$, respectively. It can be observed from Eqs. (2) and (5) that the value of $Q_{R_j}(d^k; \theta)$ in Eq. (5) can be calculated by $Q_j^k(R_j)$.

Since $Q_j^k(q)$ is the inverse function of $F_j^k(z_j^k)$, $f_j^k(z_j^k)$ and $Q_j^{k'}(q)$ are reciprocal with each other, and the entropy of Z_j^k , denote by H_j^k , can be written in terms of $Q_j^k(q)$ as follows [36]:

$$H_j^k = \int_{-\infty}^{+\infty} \left\{ -\ln f_j^k(z_j^k) \right\} f_j^k(z_j^k) dz_j^k = \int_0^1 \ln Q_j^{k'}(q) dq \quad (7)$$

According to MEM, the most unbiased estimation of $Q_j^k(q)$ maximizes the entropy in Eq. (7) subject to available statistical information such as central moments. Assuming the exact distribution of Z_j^k is unknown beforehand and the central moments can only be inferred from limited data of samples, it is recognized that the estimation of higher order central moment from a set of random samples tends to be biased when the sample size is small [29,32]. Therefore, instead of using central moments, L-moments are used as alternatives of the available statistical information in MEM. Let $L_{j,r}^k$ denote the r th ($r \geq 1$) order L-moment of Z_j^k which is given as [54]

$$L_{j,r}^k = \int_0^1 P_{r-1}^*(q) Q_j^k(q) dq \quad (8)$$

where $P_{r-1}^*(q)$ is the $(r-1)$ th order shifted Legendre polynomial. Define the indefinite integral as

$$K_r(q) = \int_q^1 P_{r-1}^*(v) dv \quad (9)$$

Then the integration in Eq. (8) can be further rewritten in terms of $Q_j^k(q)$ using Eq. (9) and the technique of integration by parts as follows [36]:

$$L_{j,r}^k = \int_0^1 K_r(q) Q_j^{k'}(q) dq - \left[K_r(q) Q_j^k(q) \right]_0^1 \quad (10)$$

where $\left[K_r(q) Q_j^k(q) \right]_0^1$ represents the difference of $K_r(q) Q_j^k(q)$ at q equal to 0 and 1. When only a set of random samples are available, $L_{j,r}^k$ can be estimated by sample L-moments which are calculated using order statistics [54]. Let $\theta_1, \theta_2, \dots, \theta_m$ denote the m independent and identically distributed (i.i.d.) vectors of uncertainties, and the corresponding m values of $Z_j^k = g_j(d^k; \theta)$ are denoted by $Z_{j,1}^k = g_j(d^k; \theta_1)$, $Z_{j,2}^k = g_j(d^k;$

$\theta_2)$, $Z_{j,m}^k = g_j(d^k; \theta_m)$. We further define $Z_{j,1:m}^k, Z_{j,2:m}^k, \dots, Z_{j,m:m}^k$ as the permutation of $Z_{j,1}^k, Z_{j,2}^k, \dots, Z_{j,m}^k$ in an ascending order, i.e., $Z_{j,1:m}^k \leq \dots \leq Z_{j,i:m}^k \leq \dots \leq Z_{j,m:m}^k$, and $Z_{j,i:m}^k$ is called the i th order statistic. The r th order sample L-moment of Z_j^k , denoted by $l_{j,r}^k$, can be obtained by Hosking [36]

$$l_{j,r}^k = \sum_{s=0}^{r-1} (-1)^{r-1-s} \binom{r-1}{s} \binom{r-1+s}{s} b_s \quad (11)$$

where b_s is one kind of the sample probability weighted moments (PWMs) of Z_j^{k+1} calculated as follows

$$b_s = m^{-1} \sum_{i=1}^m \frac{(i-1)(i-2)\dots(i-s)}{(n-1)(n-2)\dots(n-s)} Z_{j,i:m}^k \quad (12)$$

According to Ref. [36], the MEM estimates $Q_j^k(q)$ by maximizing the entropy defined in Eq. (7) subject to the first n_L L-moments, and the problem reads

$$\begin{aligned} &\text{Maximize} \int_0^1 \ln Q_j^{k'}(q) dq \\ &\text{subject to } l_{j,r}^k = \int_0^1 K_r(q) Q_j^{k'}(q) dq - \left[K_r(q) Q_j^k(q) \right]_0^1, r = 1, 2, \dots, n_L \end{aligned} \quad (13)$$

Note that in Eq. (13) the value of $l_{j,r}^k$ is calculated by Eqs. (11) and (12) from a set of available data. Let $h_{j,r}^k = l_{j,r}^k + \left[K_r(q) Q_j^k(q) \right]_0^1$ and rewrite problem (13) as

$$\begin{aligned} &\text{Maximize} \int_0^1 \ln Q_j^{k'}(q) dq \\ &\text{subject to } h_{j,r}^k = \int_0^1 K_r(q) Q_j^{k'}(q) dq, r = 1, 2, \dots, n_L \end{aligned} \quad (14)$$

From the definition of $K_r(q)$ in Eq. (9), it can be observed that the value of $K_r(q)$ at $q = 1$ is 0 with any arbitrary order r due to the integration range, and for $q = 0$ the value of $K_r(q)$ is also 0 for order $r \geq 2$ and $K_r(0) = 1$ for $r = 1$ due to the form of shifted Legendre polynomial. Therefore, $h_{j,r}^k$ can be reduced to $l_{j,r}^k$ for $r \geq 2$ and $l_{j,r}^k - Q_j^k(0)$ for $r = 1$.

Instead of directly solving problem (14), we seek to maximize the following Lagrangian functional of the entropy

$$\bar{H}_j^k(q) = \int_0^1 \ln Q_j^{k'}(q) dq - \sum_{r=1}^{n_L} \lambda_{j,r} \left(\int_0^1 K_r(q) Q_j^{k'}(q) dq - h_{j,r}^k \right) \quad (15)$$

where $\lambda_{j,r}$ ($r = 1, 2, \dots, n_L$) represent the unknown Lagrangian multipliers. The optimality condition (Euler-Lagrangian equation) for maximizing $\bar{H}_j^k(q)$ with respect to $Q_j^{k'}(q)$ yields the estimated $Q_j^{k'}(q)$ as

$$Q_j^{k'}(q) = 1 / \sum_{r=1}^{n_L} \lambda_{j,r} K_r(q) \quad (16)$$

and the Lagrangian multipliers in Eq. (16) are determined by finding the stationary point of the following functional:

$$\Gamma(\lambda_j) = - \int_0^1 \ln \left(\sum_{r=1}^{n_L} \lambda_{j,r} K_r(q) \right) dq + \sum_{r=1}^{n_L} \lambda_{j,r} h_{j,r}^k \quad (17)$$

where $\lambda_j = (\lambda_{j,1}, \lambda_{j,2}, \dots, \lambda_{j,n_L})$. It can be observed that the stationary point of Eq. (17) satisfies the equality constraints given in problem (13), and it can be found efficiently using numerical algorithms since Eq. (17) is a convex function. A brief proof for the convexity of Eq. (17) is given in Appendix A. Once the values of λ_j and $Q_j^{k'}(q)$ are determined, the quantile function $Q_j^k(q)$ can be obtained by integral

$$Q_j^k(q) = Q_j^k(0) + \int_0^q Q_j^k(v)dv \quad (18)$$

Because in practical the exact value of $Q_j^k(0)$ is usually unknown beforehand, one can estimate $Q_j^k(0)$ by the corresponding smallest order statistic $Z_{j,1:m}^k$, and $Q_j^k(q)$ in Eq. (18) is obtained by

$$Q_j^k(q) \approx Z_{j,1:m}^k + \int_0^q Q_j^k(v)dv \quad (19)$$

and the quantile $Q_{R_j}(d^k; \theta)$ in Eq. (5) can then be estimated as $Q_j^k(R_j) \approx Z_{j,1:m}^k + \int_0^{R_j} Q_j^k(q)dq$.

Remark 1. In this study the quantile function is obtained by integrating the corresponding derivative which is estimated using MEM subject to sample L-moment constraints. The original constrained MEM problem is first transformed to Lagrangian functional, and then the values of unknown Lagrangian multipliers are found by solving another unconstrained convex optimization problem which is similar to the traditional MEM in PDF estimation [55]. Therefore, different from the method in Ref. [23], the proposed method does not depend on the initial guess of the Lagrangian multipliers.

Remark 2. Since the value of $K_r(q)$ at $q = 1$ is 0 for any arbitrary order r , it can be expected that the estimated derivative of quantile function $Q_j^k(q) = 1/\sum_{r=1}^{n_L} \lambda_{j,r} K_r(q)$ will tend to be infinite as q approaches 1. Therefore, in the following numerical examples Eq. (19) is only integrated to $q = 0.9999$ to avoid numerical difficulty for obtaining the quantile function.

4. Shape and topology optimization of plane frames under uncertainty

Once the quantile in Eq. (5) is estimated using the proposed method in Section 3, problem (4) can be iteratively solved until the stopping condition Eq. (6) is reached. This section integrates the framework of quantile-based SORA with the shape and topology optimization of plane frames under uncertainty, and the details will be explained as follows.

Generally, in shape and topology optimization of plane frames the design variables are x - and y -coordinates \mathbf{x} and \mathbf{y} of nodes and cross-sectional areas \mathbf{A} . As for random variables, since in practical engineering the joint locations and cross-sectional areas of members in the frame structure may deviate from their corresponding nominal values due to manufacturing or on-site construction error, and uncertainty in the material property should also be considered. Therefore, in this study uncertainties are assumed to be random perturbations on \mathbf{x} , \mathbf{y} , \mathbf{A} and the vector of Young's modulus \mathbf{E} which are denoted by $\Delta\mathbf{x}$, $\Delta\mathbf{y}$, $\Delta\mathbf{A}$, and $\Delta\mathbf{E}$, respectively, and the vector of random variables is written as $\theta = (\Delta\mathbf{x}, \Delta\mathbf{y}, \Delta\mathbf{A}, \Delta\mathbf{E})$. Based on Eq. (4), the $(k+1)$ th deterministic shape and topology optimization of plane frames of quantile-based SORA can be written as

$$\begin{aligned} &\text{Minimize } W(\mathbf{x}, \mathbf{y}, \mathbf{A}) \\ &\text{subject to } g_j(\mathbf{x}, \mathbf{y}, \mathbf{A}) \leq \bar{g}_j - \bar{c}_j^{k+1}, j = 1, 2, \dots, n; \quad \underline{\mathbf{x}} \leq \mathbf{x} \leq \bar{\mathbf{x}}; \quad \underline{\mathbf{y}} \leq \mathbf{y} \leq \bar{\mathbf{y}}; \quad \underline{\mathbf{A}} \leq \mathbf{A} \leq \bar{\mathbf{A}} \end{aligned} \quad (20)$$

with $\bar{c}_j^{k+1} = Q_{R_j}(\mathbf{x}^k, \mathbf{y}^k, \mathbf{A}^k; \theta) - g_j(\mathbf{x}^k, \mathbf{y}^k, \mathbf{A}^k)$, $j = 1, 2, \dots, n$. In order to prevent the existence of extremely short members during shape optimization, the method in [49] is introduced in which the FDM is applied on an auxiliary truss structure to optimize the shape of plane frame. Let \mathbf{x}_{free} , \mathbf{y}_{free} and \mathbf{x}_{fix} , \mathbf{y}_{fix} denote the x - and y -coordinates of free nodes and fixed nodes, respectively, and \mathbf{t} be the force density vector applied on the members of auxiliary truss, problem (20) is rewritten as

$$\begin{aligned} &\text{Minimize } W(\mathbf{x}_{\text{free}}(\mathbf{t}), \mathbf{y}_{\text{free}}(\mathbf{t}), \mathbf{A}) \\ &\text{subject to } g_j(\mathbf{x}_{\text{free}}(\mathbf{t}), \mathbf{y}_{\text{free}}(\mathbf{t}), \mathbf{A}) \leq \bar{g}_j - \bar{c}_j^{k+1}, j = 1, 2, \dots, n; \quad \underline{\mathbf{t}} \leq \mathbf{t} \leq \bar{\mathbf{t}}; \quad \underline{\mathbf{A}} \leq \mathbf{A} \leq \bar{\mathbf{A}} \end{aligned} \quad (21)$$

with $\bar{c}_j^{k+1} = Q_{R_j}(\mathbf{x}_{\text{free}}^k, \mathbf{y}_{\text{free}}^k, \mathbf{A}^k; \theta) - g_j(\mathbf{x}_{\text{free}}^k, \mathbf{y}_{\text{free}}^k, \mathbf{A}^k)$, $j = 1, 2, \dots, n$. Note that in problem (21) the design variables are the force density \mathbf{t} and the cross-sectional areas \mathbf{A} , and \mathbf{x}_{free} and \mathbf{y}_{free} can be determined by solving the equilibrium equations with a given \mathbf{t} [49].

Remark 3. The force density method is applied on an auxiliary truss structure for determining the shape of plane frame, and it is irrelevant to the true loading and boundary conditions of the frame to be optimized in the quantile-based SORA procedure.

Remark 4. Unlike the conventional formulation of force density method [40], in this study the fixed nodes consist of the supported nodes and loaded nodes, as well as the nodes for specific reason, e.g., requirement of structural shape that are not allowed to move in any directions during the optimization process [33,35].

5. Benchmark and numerical examples

In this section one benchmark example and four numerical examples are presented to investigate the effectiveness of the proposed method. In the benchmark example the accuracy of the quantile estimation given in Sec.3 is verified by approximating the quantile function of a random variable, where the first three L-moments are used in MEM as constraints, and the results in Refs. [32,33] are also given for comparison purpose. For the four numerical examples the deterministic optimization problem (4) of quantile-based SORA is solved by sequential quadratic programming (SQP) using *fmincon* with default settings in the Optimization Toolbox of MATLAB 2018a [56], and the first four sample L-moments (i.e., $n_L = 4$) are used in MEM to estimate the derivative of quantile function in Eq. (14) with sample size $m = 50$. The first numerical example is to compare the proposed method with other existing methods on efficiency and accuracy, which has been studied in Ref. [23]. The second numerical example is an optimization of cantilever frame structure to investigate the effectiveness of proposed method for shape and topology optimization, as well as the introduction of FDM to prevent melting nodes during optimization procedure. To explore how the stopping criterion Eq. (6) works to avoid obtaining conservative result, a bridge frame structure is optimized with five displacement constraints in numerical example 3, and in the final numerical example, an L-shaped structure with 72 members is optimized to demonstrate the validity of the proposed method on handling problem with relatively large number of uncertainties. The calculations of the first four sample L-moments are given in Appendix B for convenient reference. The MCS with sample size $m_{\text{MCS}} = 1 \times 10^5$ is implemented in the numerical examples to investigate the accuracy of quantile estimation by MEM using sample L-moments, and the result at the initial iteration is also presented in order to compare it with the solution at the final iteration.

Assuming that the fixed nodes are precisely located for simplicity, the uncertainties in x - and y -coordinates are only considered in the free nodes and denoted as $\Delta\mathbf{x}_{\text{free}}$ and $\Delta\mathbf{y}_{\text{free}}$, respectively, and therefore the vector of random variables is given as $\theta = (\Delta\mathbf{x}_{\text{free}}, \Delta\mathbf{y}_{\text{free}}, \Delta\mathbf{A}, \Delta\mathbf{E})$. However, it is also possible to add uncertainties to the x - and y -coordinates of fixed nodes to simulate the variations such as installation error at the support in practical engineering. The random variables are characterized by uniformly distributed random variables, i.e., $\Delta\mathbf{x}_{\text{free}} \in [\Delta\mathbf{x}_{\text{free,lower}}, \Delta\mathbf{x}_{\text{free,upper}}]$, $\Delta\mathbf{y}_{\text{free}} \in [\Delta\mathbf{y}_{\text{free,lower}}, \Delta\mathbf{y}_{\text{free,upper}}]$, $\Delta\mathbf{A} \in [\Delta\mathbf{A}_{\text{lower}}, \Delta\mathbf{A}_{\text{upper}}]$ and $\Delta\mathbf{E} \in [\Delta\mathbf{E}_{\text{lower}}, \Delta\mathbf{E}_{\text{upper}}]$, and the subscripts of lower and upper represent the lower and upper bounds, respectively, for the corresponding uncertainties. Moreover, each member is modeled by one Euler-Bernoulli

beam element which has a solid circular cross-section, and thereby the second moment of inertia can be expressed by its cross-sectional area only. The parameter values listed in Table 1 are used for the three numerical examples of shape and topology optimization of plane frames if not specified explicitly, where $\bar{1}$ is the vector with all entries equal to 1. Flowchart of the proposed quantile-based SORA is given in Fig. 2.

5.1. Benchmark example

In this example the accuracy of the quantile estimation using the proposed method is examined with known distribution information. Consider a random variable Z with generalized Pareto distribution (GPD) whose CDF $F_{(\mu,\sigma,\xi)}(z)$ and quantile function $Q_{(\mu,\sigma,\xi)}(q)$ are given as [54]

$$F_{(\mu,\sigma,\xi)}(z) = \begin{cases} 1 - \left(1 + \frac{\xi(z-\mu)}{\sigma}\right) & \text{for } \xi \neq 0 \\ 1 - \exp\left(-\frac{z-\mu}{\sigma}\right) & \text{for } \xi = 0 \end{cases} \quad (22)$$

$$Q_{(\mu,\sigma,\xi)}(q) = \begin{cases} \mu + \frac{\sigma(1 - (1-q)^\xi)}{\xi} & \text{for } \xi \neq 0 \\ \mu - \sigma \log(1-q) & \text{for } \xi = 0 \end{cases} \quad (23)$$

where μ , σ and ξ are the location parameter, scale parameter and shape parameter, respectively. Given that $\mu = 0$, $\xi = 0.2$ and $\sigma = 1$, the exact quantile function of GPD is plotted in Fig. 3 in which a semi-log plot of probability of exceedance versus the quantile is presented, along with the approximation results obtained in Refs. [32,33] with first three integer PWM (IPWM) and fractional PWM (FPWM), which are denoted as Q_{IPWM} and Q_{FPWM} , respectively, and explicitly expressed as follows

$$Q_{IPWM}(q) = \exp(-2.0011 + 2.2061q + 1.5813q^2) \quad (24)$$

$$Q_{FPWM}(q) = 1.25 \exp(3.1778 - 2.1351(1-q)^{1.9947} - 3.7477(1-q)^{0.2162}) \quad (25)$$

By using the proposed method in Section 3, the derivative of quantile function $Q'_{MEM}(q)$ is estimated by using the first three L-moments as

$$Q'_{MEM}(q) = \frac{1}{0.9397(1-q) - 0.0870u(1-q) - 0.3836u(1-q)(2q-1)} \quad (26)$$

and the corresponding quantile function $Q_{MEM}(q)$ is obtained by integration using Eq. (19) with $Q_{MEM}(0) = 0$ and the result is also plotted

Table 1

Parameter settings of the shape and topology optimization of plane frames.

Parameters	Numerical example 2, 3 and 4
Lower bound $\Delta x_{free,lower}$ (m)	$-0.02\bar{1}$
Upper bound $\Delta x_{free,upper}$ (m)	$0.02\bar{1}$
Lower bound $\Delta y_{free,lower}$ (m)	$-0.02\bar{1}$
Upper bound $\Delta y_{free,upper}$ (m)	$0.02\bar{1}$
Lower bound ΔA_{lower} (m ²)	$-0.02A$
Upper bound ΔA_{upper} (m ²)	$0.02A$
Lower bound ΔE_{lower} (m ²)	$-0.05E$
Upper bound ΔE_{upper} (m ²)	$0.05E$
Nominal value of E (Pa)	$3 \times 10^{11}\bar{1}$
Sample size m of sample L-moments	50
Sample size m_{MCS} of MCS	1×10^5
Upper bound \bar{A} (m ²)	$0.02\bar{1}$
Lower bound \underline{A} (m ²)	$1 \times 10^{-7}\bar{1}$
Upper bound \bar{i} (N/m)	$1000\bar{1}$
Lower bound \underline{i} (N/m)	$-1000\bar{1}$

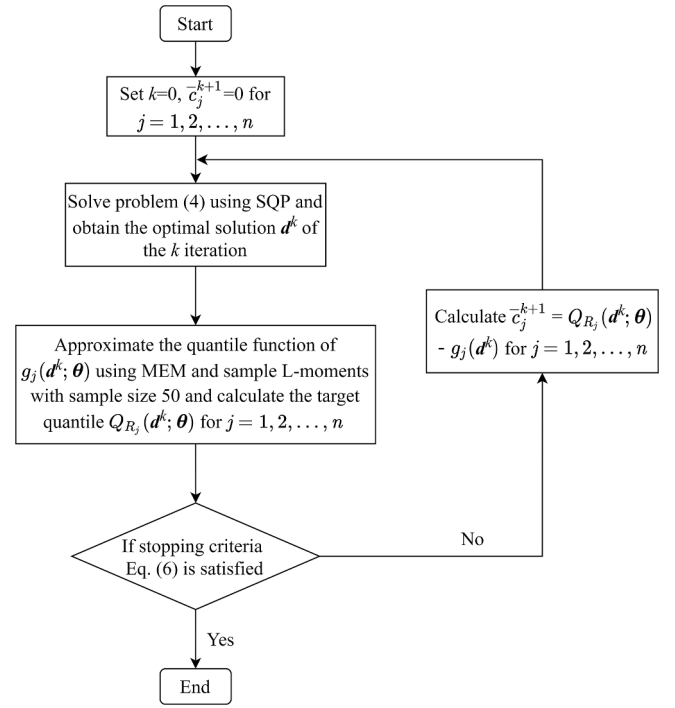


Fig. 2. Flowchart of quantile-based sequential reliability optimization.

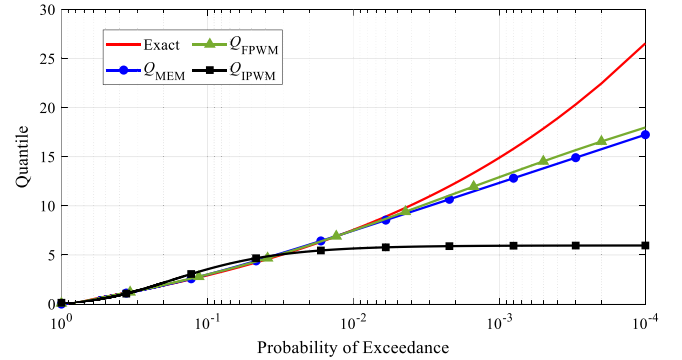


Fig. 3. Estimation of quantile function of GPD.

in Fig. 3 denoted as Q_{MEM} . It can be seen that the Q_{IPWM} is unable to appropriate the tail of GPD when the probability of exceedance is smaller than 10^{-1} , while Q_{FPWM} and Q_{MEM} have similar accuracy and can accurately estimate the tail of GPD till exceedance probability equals to 10^{-2} . However, since the Lagrangian multipliers and orders of fractional moments in Q_{FPWM} are obtained by solving a two-level nested optimization problem in Ref. [33], the result obtained by Q_{FPWM} may be sensitive to the initial guess of orders of fractional moments [23]. By contrast, the proposed method only need to solve a single convex optimization problem to obtain the unknown Lagrangian multipliers which is easy to implement and can be solved efficiently by a nonlinear programming methods without sacrificing the accuracy.

5.2. Numerical example 1

A roof truss example with six random variables and one nonlinear constraint in Ref. [23] is investigated. The RBDO problem is given as follows:

$$\begin{aligned}
&\text{find: } \mathbf{d} = [A_c, A_s] \\
&\text{min: } C(\mathbf{d}) = 364A_c + 20224A_s \\
&\text{s.t. Prob} \left[0.03 - \frac{ql^2}{2} \left(\frac{3.81}{A_c E_c} + \frac{1.13}{A_s E_s} \right) \leq 0 \right] \leq \Phi(-\beta); \beta = 3 \\
&0.018 \leq A_c \leq 0.063; 0.0006 \leq A_s \leq 0.0012; [A_c, A_s]^0 = [0.042, 0.001]
\end{aligned} \quad (27)$$

where A_c and A_s are the cross-sectional areas of reinforced concrete bars and the steel bars, respectively, and the superscript 0 in $[A_c, A_s]^0$ represents the initial values of A_c and A_s ; E_c and E_s are Young's modulus of concrete and steel, respectively; q is the uniformly distributed load, and l is the length of span of the roof truss; β is the Hasofer-Lind and Rackwitz-Fiessle (HL-RF) reliability index and Φ is the CDF of standard normal variable. The statistical properties of the random variables are tabulated in Table 2, in which DV means design variable.

According to Eq. (27) the failure probability of constraint function is 0.0013, and therefore the corresponding target probability for the quantile of constraint function is 0.9987. The results obtained by various methods in Ref. [23] and the proposed method are listed in Table 3, including the number of function calls. As can be seen from Table 3, because both H-PMA and H-SORA use first-order reliability method (FORM) for searching the most probable target point (MPTP), the constraint function is approximated by the first-order Taylor expansion to calculate the structural reliability and HF-RL reliability index which overestimates the real structural reliability index obtained by MCS in this example. Therefore, H-PMA and H-SORA converge to the similar result with $\beta^{\text{MCS}} = 2.90$ which is less than the requirement in problem (27). On the other hand, the result obtained by the proposed method is close to the one obtained by Ref. [23] with slightly larger objective function value, and both of them have larger β^{FORM} than the requirement.

The iteration histories of the objective function value and the quantile of the constraint function obtained by the proposed method are also shown in Fig. 4. It can be observed that the proposed method converges at iteration 5 and the total number of function evaluations is $123 + 6 \times 50 = 423$ with sample size 50 for evaluating the sample L-moments at iteration, where 123 is the number of function evaluations in all processes of deterministic optimization. Compared to the results in Ref. [23], the total number of function evaluations of the proposed method is a little smaller than that in Ref. [23], while the method in Ref. [23] needs only 4 iterations for solving the optimization problem. The main reason would be that the method in Ref. [23] calculates the fractional moments using sparse grid numerical integration (SGNI) or univariate dimension-reduction method (UDRM) in which the number of sample points needed in the calculation is positively related to the number of random variables. For this example 97 samples are needed in each iteration to calculate the Laplace transform of PDF of constraint function with 6 random variables. On the other hand, in the proposed method, since the L-moments are calculated from observed samples, the number of sample points for each iteration is predefined and independent of the number of random variables. Therefore, although for problem (27) the proposed method needs more iterations to converge to the final result than that in Ref. [23], the total number of function evaluations are slightly smaller than that in Ref. [23], and this tendency is expected to become stronger when the number of random variables

Table 2
Statistical information of random variables.

Variable	q (N/m)	l (m)	A_c (m ²)	A_s (m ²)	E_c (Pa)	E_s (Pa)
Distribution	Normal	Normal	Normal	Normal	Normal	Normal
Mean	20,000	12	DV	DV	2×10^{10}	1×10^{11}
Standard deviation	1400	0.12	4.8×10^{-3}	5.892×10^{-5}	1.2×10^9	6×10^9

Table 3
Results of different methods.

Method	H-PMA	H-SORA	Ref. [23]	Proposed
Number of function calls	1495	1321	458	423
Optimal value of design variable	3.8358×10^{-2}	3.8312×10^{-2}	3.5702×10^{-2}	3.5724×10^{-2}
Optimal objective value	35.9785	35.9765	36.5889	36.6103
β^{MCS}	2.90	2.90	2.99	3.00
β^{FORM}	3.0105	3.0230	3.1558	3.1623

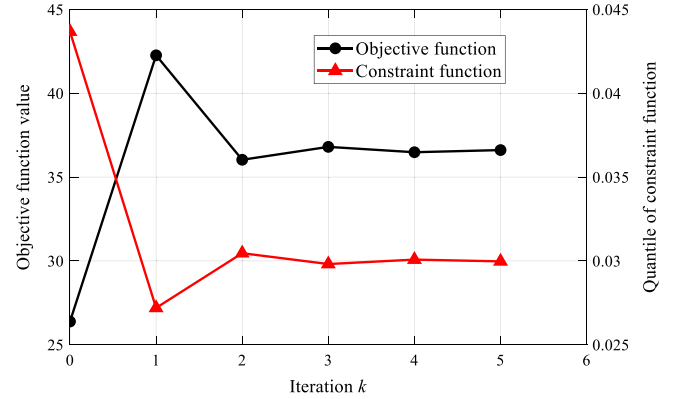


Fig. 4. Iteration history of objective function and 0.9987th quantile of constraint function.

increases.

5.3. Numerical example 2

This example includes a 3×2 grid cantilever frame with 12 nodes and 27 members, and the initial structure is shown in Fig. 5. The structure is pin-supported at nodes 1, 2 and 3 and a downward vertical load $F = 1000$ kN is applied at node 11; therefore the fixed nodes for FDM are selected as nodes 1, 2, 3 and 11. Based on Eq. (3), the optimization problem is formulated to minimize the structural volume subject to reliability constraint on the downward vertical displacement of node 11. The optimization problem is formulated as

$$\begin{aligned}
&\text{Minimize } W(\mathbf{x}_{\text{free}}(t), \mathbf{y}_{\text{free}}(t), \mathbf{A}) \\
&\text{subject to } Q_{R_{11}}(\mathbf{x}_{\text{free}}(t), \mathbf{y}_{\text{free}}(t), \mathbf{A}; \boldsymbol{\theta}) \leq 3 \times 10^{-3} \text{ m}; \underline{t} \leq t \leq \bar{t}; \underline{A} \leq A \leq \bar{A}
\end{aligned} \quad (28)$$

where W is the structural volume; $Q_{R_{11}}$ is the quantile of vertical displacement of node 11 with target probability $R_{11} = 0.99$. According to Eq. (21), the quantile-based SORA of problem (28) can be written as

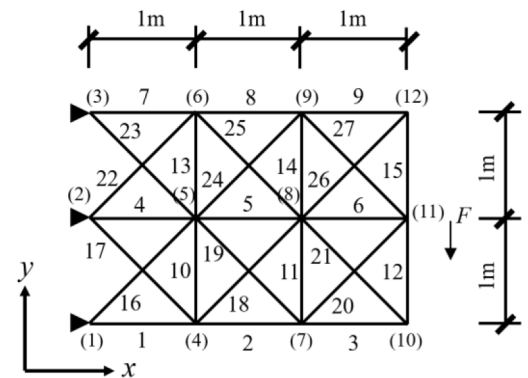


Fig. 5. Initial structure of example 2.

$$\begin{aligned} & \text{Minimize } W(\mathbf{x}_{\text{free}}(\mathbf{t}), \mathbf{y}_{\text{free}}(\mathbf{t}), \mathbf{A}) \\ & \text{subject to } g_{11}(\mathbf{x}_{\text{free}}(\mathbf{t}), \mathbf{y}_{\text{free}}(\mathbf{t}), \mathbf{A}) \leq 3 \times 10^{-3} - \bar{c}_{11}^{k+1}; \quad \mathbf{t} \leq \mathbf{t}^k; \quad \mathbf{A} \leq \mathbf{A}^k \end{aligned} \quad (29)$$

where g_{11} is the vertical displacement of node 11 without considering uncertainty, and \bar{c}_{11}^{k+1} is the shifting value on the upper bound of g_{11} at the $(k+1)$ th iteration. The optimization procedure converged at $k=3$, and the results at initial and final iterations are presented in Fig. 6. The structural volumes and quantiles $Q_{R_{11}}$ of the results at initial and final iterations are listed in Table 4 in which the quantiles obtained by MCS with sample size m_{MCS} are listed in the parentheses, and the corresponding nodal locations, force densities, cross-sectional areas and member lengths are also given in Tables 5 and 6, respectively. As can be seen from Fig. 7 and Tables 4–6, the results at the initial and final iterations have similar shapes, however, the cross-sectional area of each member has increased before reaching the final iteration to satisfy the displacement constraint on node 11, leading to a larger structural volume and a smaller $Q_{R_{11}}$ compared to the result at initial iteration.

Moreover, the quantile functions of vertical displacement of node 11 obtained by MCS and MEM with sample L-moments are also given in Fig. 7 for both results at initial and final iterations. It can be observed from Fig. 7(a) and Table 4 that when uncertainty is taken into consideration for the result at the initial iteration, the probability of the vertical displacement of node 11 exceeding the upper bound 3×10^{-3} m is about 0.8, which means the structure has low reliability. On the other hand, although the structural volume of result at final iteration increased about 7%, the reliability constraint on the vertical displacement of node 11 is satisfied, and the estimated quantile $Q_{R_{11}}$ using the proposed MEM is close to the one obtained by MCS where the relative error is around 2% as shown in Fig. 7(b), indicating that the proposed method is able to estimate the quantile function with satisfactory accuracy.

To further investigate the effectiveness of introducing FDM into quantile-based SORA for shape and topology optimization of plane frame, the three nodes 9, 11 and 12 are combined to a single node, and members 2, 3, 4, 6, 11, 12, 14, 17, 19, 20, 21, 22, 24 and 25, which have very small cross-sectional areas, are removed from the structure to obtain a distinct structural shape and topology as shown in Fig. 8(a). The quantile functions of vertical displacement of node 7 obtained by MCS and MEM with sample L-moments are given in Fig. 8(b). The locations of nodes, cross-sectional areas and member lengths after further modifications are listed in Tables 7 and 8, and the structural volumes, nominal values and quantiles of the displacement constraint functions before and after further modification are also given in Table 10 for comparison, in which the quantiles obtained by MCS are listed in the parentheses.

It can be observed from Table 9 that due to regularity of the stiffness matrix, the nominal value of the displacement constraint after modification is only slightly smaller than that before modification. This is

Table 4

Structural volumes and quantiles $Q_{R_{11}}$ of the results of numerical example 2 at the initial and final iterations.

Result	Initial iteration	Final iteration
Structural volume (m^3)	9.2167×10^{-2}	9.8017×10^{-2}
$Q_{R_{11}}$ (m)	3.199×10^{-3} (3.175×10^{-3})	3.0×10^{-3} (2.973×10^{-3})

Table 5

Location of nodes of the results of numerical example 2 at the initial and final iteration.

Node	Initial iteration		Final iteration	
	x-coordinate (m)	y-coordinate (m)	x-coordinate (m)	y-coordinate (m)
1	0	0	0	0
2	0	1	0	1
3	0	2	0	2
4	1.8857	0.3067	1.8852	0.3068
5	1.5154	1.0144	1.5149	1.0144
6	1.9414	1.6754	1.9409	1.6753
7	2.2633	0.4784	2.2625	0.4787
8	2.0518	0.3718	2.0511	0.3718
9	2.9785	1.0144	2.9776	1.0148
10	2.4708	0.6290	2.4701	0.6291
11	3	1	3	1
12	2.9785	0.9886	2.9777	0.9882

because the removal of thin members from the structure results in a small decrease in structural volume and stiffness. However, the quantile after modification is smaller than that before modification, resulting in a structure with a little higher reliability than the requirement. The main reason for this result is that since the closely spaced nodes are merged to a single node and thin members are removed, only 7 nodes and 10 members are left in the distinct result as displayed in Fig. 8(a) and Tables 3 and 4. Accordingly, the quantile of the stochastic displacement decreases a little after modification due to less uncertainty involved in the structure, indicating that by introducing the FDM into quantile-based SORA a feasible result can be obtained without melting nodes, and the feasibility still remains in the final distinct structure with no extremely thin members or closely space nodes. This way, an optimal shape with small numbers of nodes and members satisfying reliability constraint can easily be obtained by combining FDM and SORA method.

5.4. Numerical example 3

In the third numerical example, we investigate the optimal shape and topology of a bridge-frame with a 6×1 grid where the 14 nodes are

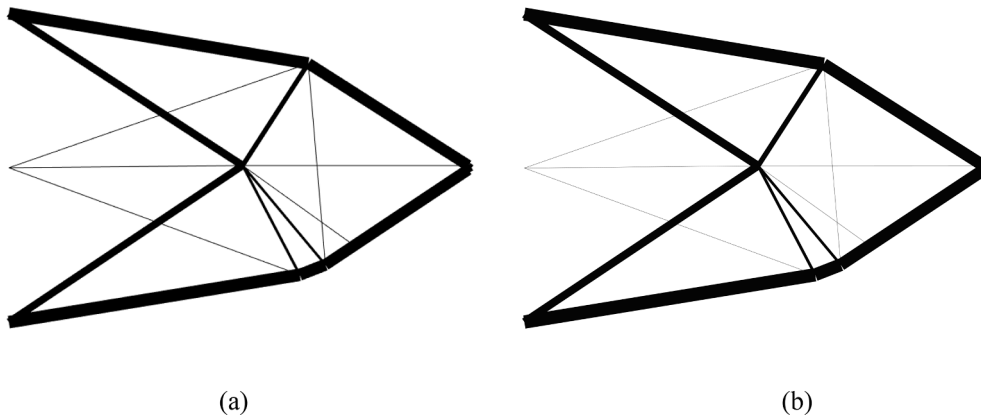
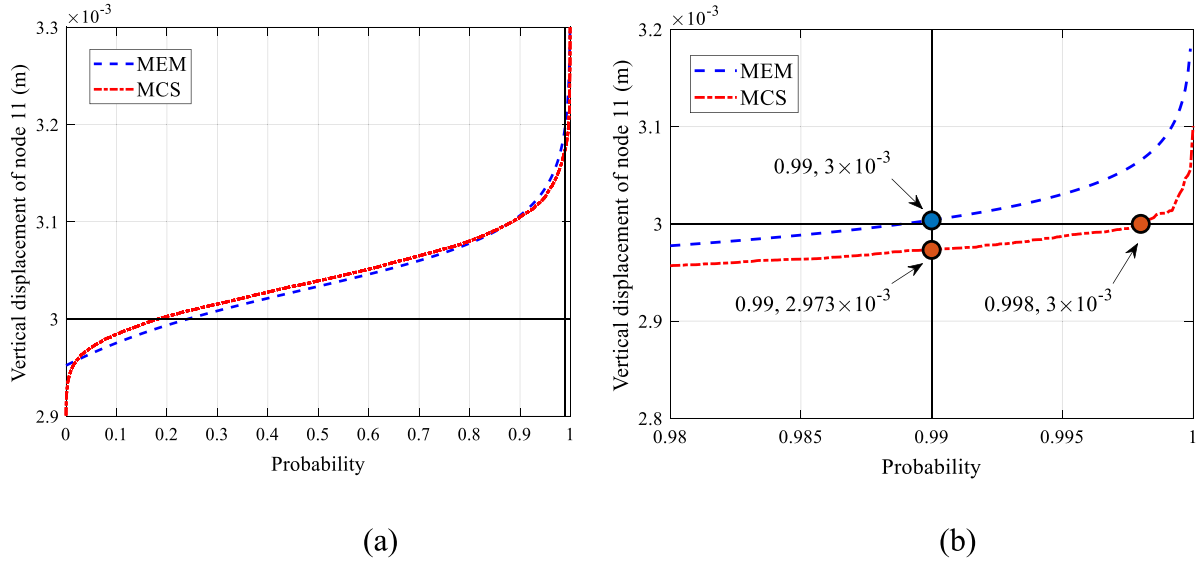


Fig. 6. Results of example 2 at: (a) initial iteration; (b) final iteration.

Table 6

Force densities, cross-sectional areas and member lengths of the results of numerical example 2 at the initial and final iterations.

Member	Initial iteration			Final iteration		
	Force density (N/m)	Cross-sectional area (m ²)	Member length (m)	Force density (N/m)	Cross-sectional area (m ²)	Member length (m)
1	0.7491	0.0102	1.9104	0.7489	0.0109	1.9101
2	1.3772	1.00×10^{-7}	0.4148	1.3774	1.00×10^{-7}	0.4146
3	0.7021	3.59×10^{-7}	0.2563	0.7021	1.00×10^{-7}	0.2563
4	0.3807	1.00×10^{-7}	1.5155	0.3809	1.00×10^{-7}	1.5150
5	0.1951	0.00207	0.8370	0.1951	0.00218	0.8368
6	0.7478	1.00×10^{-7}	1.1373	0.7484	1.00×10^{-7}	1.1379
7	-0.7517	0.0100	1.9683	-0.7516	0.0107	1.9678
8	-0.6716	0.00921	1.2298	-0.6720	0.00982	1.2293
9	-0.2787	0.00452	0.0257	-0.2788	0.00484	0.0266
10	0.2944	0.00218	0.7987	0.2942	0.00230	0.7986
11	1.0208	3.93×10^{-7}	0.2368	1.0210	3.95×10^{-7}	0.2368
12	0.3521	4.54×10^{-7}	0.6462	0.3521	1.00×10^{-7}	0.6467
13	0.2404	0.00392	0.7864	0.2402	0.00417	0.7863
14	-0.6716	1.00×10^{-7}	1.1276	-0.6710	1.00×10^{-7}	1.1277
15	-2.4518	0.00517	0.0243	-2.4517	0.00555	0.0252
16	0.2554	0.00609	1.8236	0.2553	0.00645	1.8232
17	-0.4243	1.00×10^{-7}	2.0091	-0.4243	1.00×10^{-7}	2.0086
18	1.2129	0.00977	0.1784	1.21291	0.0105	0.1782
19	-0.1673	1.00×10^{-7}	0.9201	-0.1657	1.00×10^{-7}	0.9196
20	0.6315	1.00×10^{-7}	0.9026	0.6315	1.00×10^{-7}	0.9031
21	0.0970	1.00×10^{-7}	0.4916	0.0973	1.00×10^{-7}	0.4917
22	0.3322	1.00×10^{-7}	2.0555	0.3319	1.00×10^{-7}	2.0550
23	0.3549	0.00629	1.8077	0.3553	0.00667	1.8073
24	0.8960	1.00×10^{-7}	1.4630	0.8957	1.00×10^{-7}	1.4627
25	-0.1406	1.00×10^{-7}	1.3083	-0.1404	1.00×10^{-7}	1.3082
26	-0.0568	0.00933	1.1132	-0.0589	0.00996	1.1128
27	-0.3659	0.00506	0.02588	-0.3659	0.00542	0.0268

**Fig. 7.** Quantile functions of vertical displacement of node 11 of example 2 at the results of: (a) initial iteration; (b) final iteration.

connected by 31 members, and the initial structure is shown in Fig. 9. The structure is pin-supported at node 1 and roller-supported at node 13. At each of the nodes 3, 5, 7, 9 and 11, a downward vertical load with magnitude 1000 kN is applied. Accordingly, these 7 nodes are considered as fixed nodes for shape optimization using FDM.

The optimization problem is to minimize the structural volume subject to constraints on the downward vertical displacements of nodes 3, 5, 7, 9 and 11, which should not exceed 3×10^{-3} m with target probability. Based on Eqs. (3) and (21), the original optimization problem and quantile-based SORA problem can be formulated as

$$\begin{aligned} & \text{Minimize } W(\mathbf{x}_{\text{free}}(t), \mathbf{y}_{\text{free}}(t), \mathbf{A}) \\ & \text{subject to } Q_{R_j}(\mathbf{x}_{\text{free}}(t), \mathbf{y}_{\text{free}}(t), \mathbf{A}; \theta) \leq 3 \times 10^{-3} \text{ m}, j = 3, 5, 7, 9, 11; \\ & \quad \underline{\mathbf{A}} \leq \mathbf{A} \leq \bar{\mathbf{A}}; t \leq \bar{t} \end{aligned} \quad (30)$$

$$\begin{aligned} & \text{Minimize } W(\mathbf{x}_{\text{free}}(t), \mathbf{y}_{\text{free}}(t), \mathbf{A}) \\ & \text{subject to } g_j(\mathbf{x}_{\text{free}}(t), \mathbf{y}_{\text{free}}(t), \mathbf{A}) \leq 3 \times 10^{-3} - \bar{c}_j^{k+1}, j = 3, 5, 7, 9, 11; t \leq \bar{t}; \underline{\mathbf{A}} \leq \mathbf{A} \leq \bar{\mathbf{A}} \end{aligned} \quad (31)$$

where W is the structural volume; Q_{R_j} is the quantile of vertical displacement of node j with target probability $R_j = 0.99$ ($j = 3, 5, 7, 9, 11$); g_j is the vertical displacement of node j without uncertainty, and \bar{c}_j^{k+1} is the shifting value on the upper bound of g_j at the $(k + 1)$ th

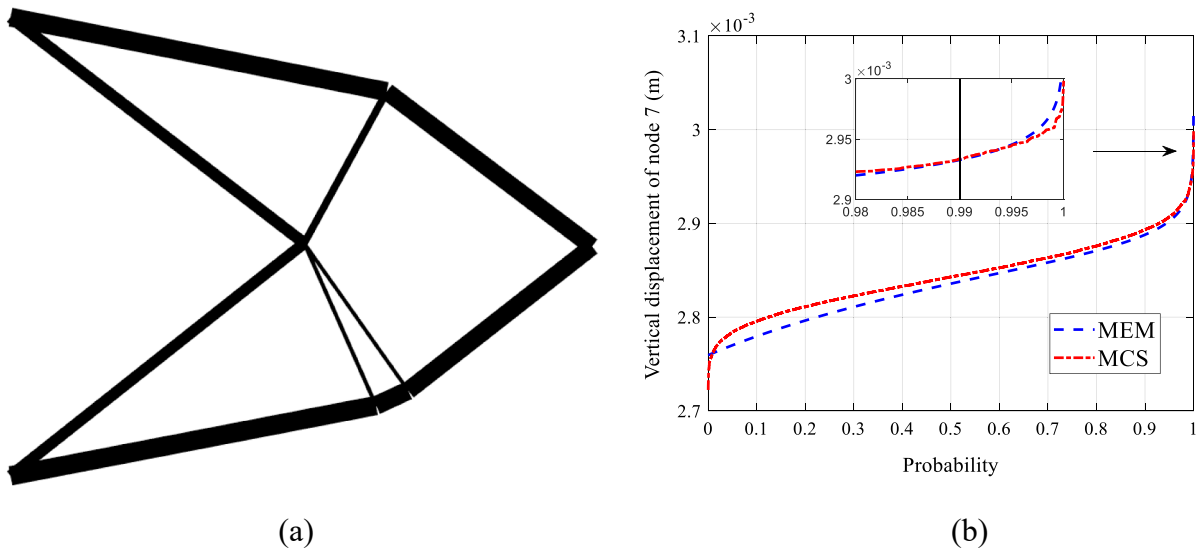


Fig. 8. Result of example 2 after further modification: (a) Optimal shape; (b) Quantile functions of vertical displacement of node 7.

Table 7

Location of nodes of optimal result of example 2 after further modification.

Node	1	2	3	4	5	6	7
x-coordinate (m)	0	0	1.8852	1.5149	1.9409	2.0511	3
y-coordinate (m)	0	2	0.3068	1.0144	1.6753	0.3718	1

Table 8

Cross-sectional areas and member lengths of optimal result of example 2 after further modification.

Element		Cross-sectional area (m ²)	Member length (m)
Node 1	Node 2		
1	3	0.0109	1.9100
4	6	0.00218	0.8368
2	5	0.0107	1.9678
5	7	0.00982	1.2293
3	4	0.00230	0.7986
4	5	0.00417	0.7863
1	4	0.00645	1.8232
3	6	0.0105	0.1782
2	4	0.00667	1.8073
6	7	0.00996	1.1128

Table 9

Structural volumes, quantiles and nominal values of constraints of example 2 before and after further modification.

Result	Before modification	After modification
Structural volume (m ³)	9.8017×10^{-2}	9.8016×10^{-2}
Nominal value of constraint (m)	2.820×10^{-3}	2.828×10^{-3}
Quantile of constraint (m)	3.0×10^{-3} (2.973 $\times 10^{-3}$)	2.932×10^{-3} (2.933 $\times 10^{-3}$)

iteration.

The optimization procedure converged at $k = 34$, and the results at the initial and final iterations are shown in Fig. 10. Table 10 shows the structural volumes and quantiles of the results at initial and final iterations where the quantiles obtained by MCS are listed in the parentheses, and the corresponding locations of nodes, force densities, cross-sectional areas and member lengths of the results at initial and final iterations are listed in Tables 11 and 12, respectively. We can see from Fig. 10(a) and Tables 11 and 12 that the structure obtained at the initial

Table 10

Structural volumes and quantiles Q_{R_j} of the results of numerical example 3 at the initial and final iterations.

Result	Initial iteration	Final iteration
Structural volume (m ³)	0.2728	0.3861
Q_{R_3} (m)	4.490×10^{-3} (4.516×10^{-3})	2.926×10^{-3} (2.840×10^{-3})
Q_{R_5} (m)	4.962×10^{-3} (4.625×10^{-3})	3.0×10^{-3} (2.954×10^{-3})
Q_{R_7} (m)	3.866×10^{-3} (3.988×10^{-3})	2.992×10^{-3} (2.908×10^{-3})
Q_{R_9} (m)	4.883×10^{-3} (4.606×10^{-3})	2.994×10^{-3} (2.936×10^{-3})
$Q_{R_{11}}$ (m)	4.866×10^{-3} (4.502×10^{-3})	2.993×10^{-3} (2.974×10^{-3})

iteration is unstable in horizontal direction if the bending stiffness is small, and therefore the quantiles of displacements of nodes 3, 5, 7, 9 and 11 are significantly larger than 3×10^{-3} m as shown in Table 10. The quantile functions of the displacements of these five nodes obtained by the proposed MEM and MCS are presented in Fig. 11(a) for the result at initial iteration, and it can be observed that the upper bound of the displacements 3×10^{-3} m only corresponds to the probability about 0.4 for these five quantile functions, while the quantile functions obtained by the proposed MEM approximately fit those obtained by MCS. Moreover, the quantile Q_{R_7} of node 7 is smaller than other quantiles Q_{R_j} of the other four nodes 3, 5, 9 and 11, which are indicated by the vertical line in Fig. 11(a). The main reason for this would be that node 7 is symmetrically connected by two thick horizontal members 12 and 17 and one vertical member 16, making the nodal stiffness less sensitive to the asymmetric uncertainties.

On the contrary, the result at the final iteration is stable in both vertical and horizontal directions due to the increase of cross-sectional areas of members 2 and 27 as shown in Fig. 10(b) and Tables 11 and 12, and its shape and topology are also changed rather than simply increasing the cross-sectional areas of the result at initial iteration as in example 1. Fig. 11(b) displays the quantile functions of vertical displacements of nodes 3, 5, 7, 9 and 11 of the result at final iteration. We can see from Table 10 and Fig. 11(b) that the quantile functions obtained by the proposed MEM with sample L-moments are close to those obtained by MCS where the relative error is around 3%. The equality holds for the displacement constraint of node 5, while the constraints of other

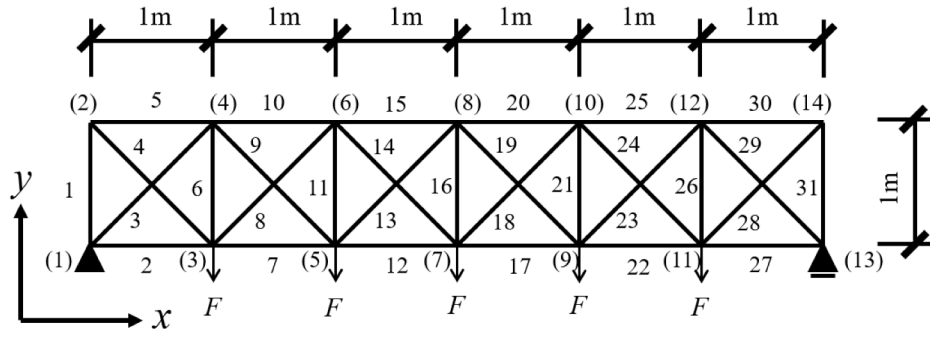


Fig. 9. Initial structure of example 3.

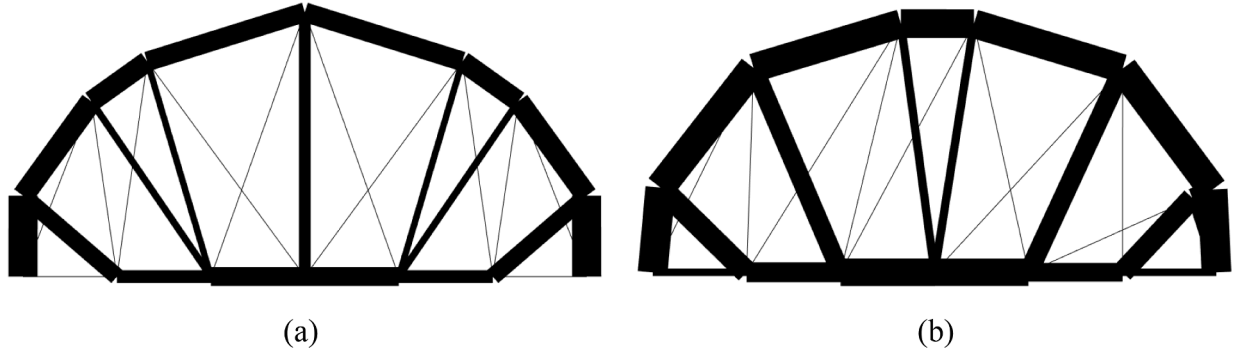


Fig. 10. Results of example 3 at: (a) initial iteration; (b) final iteration.

Table 11

Location of nodes of the results of numerical example 3 at initial and final iterations.

Node	Initial iteration		Final iteration	
	x-coordinate (m)	y-coordinate (m)	x-coordinate (m)	y-coordinate (m)
1	0	0	0	0
2	0.00161	0.8611	0.0817	0.9028
3	1	0	1	0
4	0.7276	1.8660	1.0733	2.1766
5	2	0	2	0
6	1.3225	2.2903	2.6415	2.6477
7	3	0	3	0
8	3.0000	2.8149	3.4190	2.6472
9	4	0	4	0
10	4.6772	2.2904	5.0011	2.1695
11	5	0	5	0
12	5.2722	1.8662	5.9590	0.8813
13	6	0	6	0
14	5.9984	0.8611	5.7428	0.7927

four nodes are also satisfied with slightly higher reliability than the requirement.

Furthermore, Fig. 12 displays the iteration histories of the total structural volume, which is the objective function, and the maximum value of the five quantiles Q_{R_i} of the vertical displacements of nodes 3, 5, 7, 9 and 11 to illustrate how Eq. (6) prevents obtaining the conservative result. As shown in Figs. 10 and 12, since the result at initial iteration is unstable in y-direction when the bending stiffness is small, the maximum value of the five quantiles Q_{R_i} at $k = 0$ is about 0.49 and large shifting values would be applied to the upper bounds of constraints for the next iteration where an extremely narrow feasible domain is constructed. Therefore, it can be expected that the result at $k = 1$ would have large structural volume to satisfy the constraints, and as displayed in Fig. 12 the maximum value of the five quantiles Q_{R_i} for $k = 1$ is far less than $3 \times$

10^{-3} m which indicates the result is highly reliable. In order to prevent obtaining such conservative result, the upper bounds of the constraints for the next iteration are relaxed by shifting values using Eq. (5), and we can see from Fig. 12 that the structural volume of the result at $k = 2$ is reduced compared to that at $k = 1$, but the maximum value of the five quantiles Q_{R_i} also increases and exceeds 3×10^{-3} m. Hence, the quantile-based SORA optimization procedure keeps going until Eq. (6) is reached, where the structural volume and the maximum value of the five quantiles Q_{R_i} increases and decreases alternatively. In this example the proposed method converged to the final result at $k = 34$ where all the constraints are satisfied and at least one of them holds equality, however, the structural volume is significantly reduced compared to the result at $k = 1$, showing that instead of obtaining a conservative result, a result with smaller objective value which satisfies all the reliability constraints can be found by using Eq. (6) as stopping criteria.

5.5. Numerical example 4

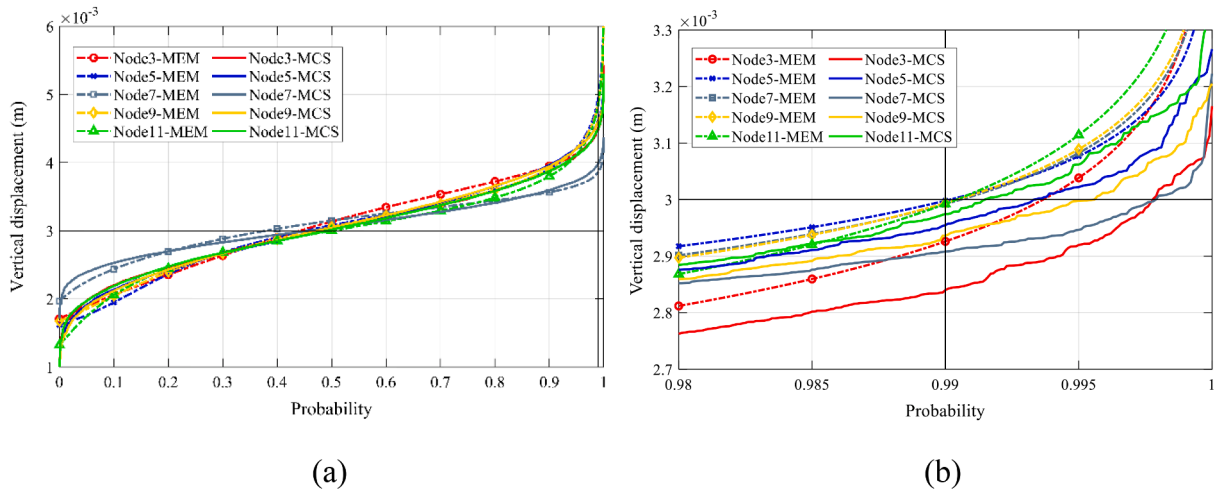
The last example is an L-shape frame with 27 nodes and 72 members, and the initial shape is shown in Fig. 13(a). The structure is pin-supported at nodes 1, 2 and 3 and a downward vertical load F with magnitude 1000 kN is applied at node 25. Because the optimal result is expected to be an L-shape frame, node 15, as well as nodes 1, 2, 3 and 25, are classified as fixed nodes, and the remaining 22 nodes are free nodes in the process of shape optimization using FDM. Similarly, the optimization problem is to minimize the structural volume subject to displacement constraint on node 25. According to Eqs. (3) and (21), the original and SORA quantile-based optimization problems can be written as

$$\begin{aligned} & \text{Minimize } W(\mathbf{x}_{\text{free}}(\mathbf{t}), \mathbf{y}_{\text{free}}(\mathbf{t}), \mathbf{A}) \\ & \text{subject to } Q_{R_{25}}(\mathbf{x}_{\text{free}}(\mathbf{t}), \mathbf{y}_{\text{free}}(\mathbf{t}), \mathbf{A}; \boldsymbol{\theta}) \leq 3 \times 10^{-3} \text{ m;} \\ & \quad \mathbf{t} \leq \bar{\mathbf{t}}; \quad \mathbf{A} \leq \bar{\mathbf{A}} \end{aligned} \quad (32)$$

Table 12

Force densities, cross-sectional areas and member lengths of the results of numerical example 3 at initial and final iterations.

Member	Initial iteration			Final iteration		
	Force density (N/m)	Cross-sectional area (m ²)	Member length (m)	Force density (N/m)	Cross-sectional area (m ²)	Member length (m)
1	-4.2451	0.01950	0.8611	-8.0102	0.0200	0.9065
2	-0.4437	1.00×10^{-7}	1	-1.6791	0.005013	1
3	0.6192	1.00×10^{-7}	2.0029	2.1740	1.00×10^{-7}	2.4269
4	0.4073	0.01138	1.3184	-2.1750	0.01529	1.2878
5	0.30179	0.01476	1.2397	0.3018	0.02	1.6143
6	1.4748	1.00×10^{-7}	1.8858	6.1282	1.00×10^{-7}	2.1779
7	0.6607	0.00854	1	2.3062	0.01335	1
8	-0.9181	1.00×10^{-7}	2.3129	-3.9185	1.00×10^{-7}	3.1153
9	1.5906	0.004665	2.2585	0.78232	0.01277	2.3657
10	-0.1634	0.01388	0.7306	-0.1635	0.01931	1.6374
11	-0.4086	0.00433	2.3884	4.0304	1.00×10^{-7}	2.7243
12	2.7744	0.01255	1	6.5428	0.01847	1
13	-0.3667	1.00×10^{-7}	2.9873	-4.2966	1.00×10^{-7}	3.0036
14	-0.0961	1.00×10^{-7}	2.8389	2.1693	0.005614	2.6719
15	-0.0376	0.01315	1.7576	-0.0375	0.01925	0.7775
16	-0.06201	0.007858	2.8149	-4.9602	0.005586	2.6802
17	1.5919	0.01255	1	1.6626	0.01834	1
18	0.6089	1.00×10^{-7}	2.8388	3.8661	1.00×10^{-7}	2.9515
19	-0.2899	1.00×10^{-7}	2.9873	0.8785	1.00×10^{-7}	2.7103
20	0.2262	0.01314	1.7573	0.2263	0.01919	1.6526
21	-0.7517	0.004327	2.3884	-2.6384	0.01302	2.3894
22	-0.6006	0.008546	1	-4.9624	0.01254	1
23	1.8957	0.004668	2.2586	4.9905	1.00×10^{-7}	2.1482
24	0.6664	1.00×10^{-7}	2.3131	3.3449	1.00×10^{-7}	2.1695
25	-0.02156	0.01388	0.7307	-0.0215	0.0200	1.6053
26	0.01296	1.00×10^{-7}	1.8859	-1.2331	1.00×10^{-7}	1.3025
27	0.2494	1.00×10^{-7}	1	1.0612	0.005001	1
28	-0.6394	0.01138	1.3184	-6.5217	0.01441	1.0864
29	-0.3378	1.00×10^{-7}	2.0031	1.0221	0.0200	0.8823
30	0.1868	0.01476	1.23999	0.1868	0.01251	0.2336
31	-2.1711	0.01950	0.86109	-4.2898	0.006430	0.8334

**Fig. 11.** Quantile functions of vertical displacement of nodes 3, 5, 7, 9 and 11 of example 3 at the results of: (a) initial iteration; (b) final iteration.

$$\begin{aligned} & \text{Minimize } W(\mathbf{x}_{\text{free}}(t), \mathbf{y}_{\text{free}}(t), \mathbf{A}) \\ & \text{subject to } g_{25}(\mathbf{x}_{\text{free}}(t), \mathbf{y}_{\text{free}}(t), \mathbf{A}) \leq 3 \times 10^{-3} - \bar{c}_{25}^{k+1}; \quad t \leq t \leq \bar{t}; \quad \mathbf{A} \leq \mathbf{A} \leq \bar{\mathbf{A}} \end{aligned} \quad (33)$$

where $Q_{R_{25}}$ is the quantile of the vertical displacement of node 25 with target probability $R_{25} = 0.99$; g_{25} is the vertical displacement of node 25 without uncertainty; \bar{c}_{25}^{k+1} is the shifting value on upper bound of g_{25} at $(k + 1)$ th iteration. The quantile-based SORA optimization procedure converged at $k = 16$, and the results of problem (34) at the initial and final iterations are displayed in Fig. 13(b) and (c), respectively. The structural volumes and quantiles $Q_{R_{25}}$ at the results of initial and final iterations are listed in Table 13 where those obtained by MCS are shown within the parentheses, and the corresponding quantile functions are

also shown in Fig. 14. The location of nodes of the results at the initial and final iterations are listed in Table 14, and for simplicity the corresponding force densities, cross-sectional areas and member lengths of each member are not given for this example.

Compared to the result at initial iteration, the shape of the result at final iteration has been changed a little and some of the members have increased their cross-sectional areas. It can be seen from Fig. 14 that the result at initial iteration is very unreliable since the probability of displacement of node 25 less than 3×10^{-3} m is less than 0.1, indicating that the constraint would not be satisfied at most of the cases when uncertainty is considered. By contrast, for the result at final iteration the quantile $Q_{R_{25}}$ is equal to 3×10^{-3} m, providing a more reliable structure with a slightly larger structural volume as listed in Table 13.

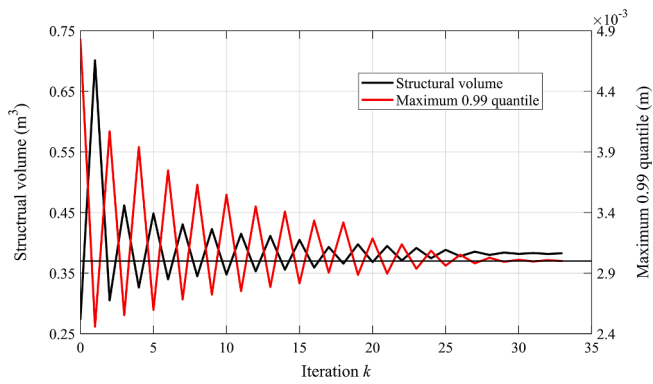


Fig. 12. Iteration histories of objective and maximum 0.99th quantile of constraints.

It should be noted that since the uncertainties in Eq. (34) involve randomness in x - and y -coordinates of free nodes Δx_{free} and Δy_{free} , and randomness in cross-sectional area ΔA and Young's modulus ΔE of each member, the total number of uncertainties is $22 + 22 + 72 + 72 = 188$. However, in this example the number of samples for calculating sample L-moments are still limited to 50 which is the same as in numerical examples 1–3, and the accuracy of quantile estimation is not influenced by the increase of total number of uncertainties. The main reason would be that in the proposed method the random structural response is regarded as one random variable, and its distribution is estimated using the sample L-moments which is less sensitive to the sample size, thus the estimation accuracy is not related to the number of uncertainties, whereas for surrogate model aided method one need to characterize the complicated relationship between input uncertainty and output random structural response, and the number of training samples will increase as the number of uncertainties increases in order to ensure the approximation accuracy [57].

6. Conclusions

In this paper a new quantile-based SORA method has been proposed for shape and topology optimization of plane frames. The shifting value on the upper bound of response is calculated in terms of quantile. The MEM is integrated to estimate the derivative of quantile function of the performance function in which the sample L-moments are used due to its

less variability to the sample size. An unconstrained convex optimization problem is formulated and solved to determine the unknown Lagrangian multipliers. The quantile function can then be obtained by integrating the corresponding derivative. Because the derivative of quantile function will become infinity as the probability approaches 1, the quantile function is only obtained up to the probability of 0.9999 in order to avoid numerical difficulty in integration. Besides, the FDM is also introduced for shape optimization to alleviate the difficulty caused by the existence of extremely short member. In order to prevent obtaining conservative result, the quantile-based SORA is considered convergent and stopped if all the constraints are satisfied and at least one of them holds equality.

One benchmark example and four numerical examples have been presented to investigate and illustrate the effectiveness of the proposed method. In the benchmark example the quantile function of generalized Pareto distribution is estimated by the proposed MEM with L-moments, and other two estimation methods using integer and fractional PWM are also applied for comparison purpose. The result shows that the proposed MEM is more accurate than the method using integer PWM at the tail of distribution. Although the proposed method and the method using fractional PWM have similar estimation accuracy, the proposed method is easier to implement because it does not need to solve a double-loop optimization problem where the initial guess of the order of fractional moments has a great influence on the quantile approximation.

Four numerical examples, including one mathematical problem and three structural optimization problems, have been presented to investigate the effectiveness of the proposed quantile-based SORA. The sample size for calculating the sample L-moments are all set to 50. In the mathematical problem, it is shown that the result obtained by the proposed method is close to the result in previous study with a slightly larger objective values, and the quantile function calculated by MCS can be estimated by the proposed MEM subject to the constraints on the first four sample L-moments without difficulty. It is interested to note that for traditional reliability-based optimization using HL-RF index the

Table 13

Structural volumes and quantiles $Q_{R_{25}}$ of the results of numerical example 4 at the initial and final iterations.

Result	Initial iteration	Final iteration
Structural volume (m^3)	0.6349	0.6957
$Q_{R_{25}}$ (m)	3.187×10^{-3} (3.184×10^{-3})	3.0×10^{-3} (2.9×10^{-3})

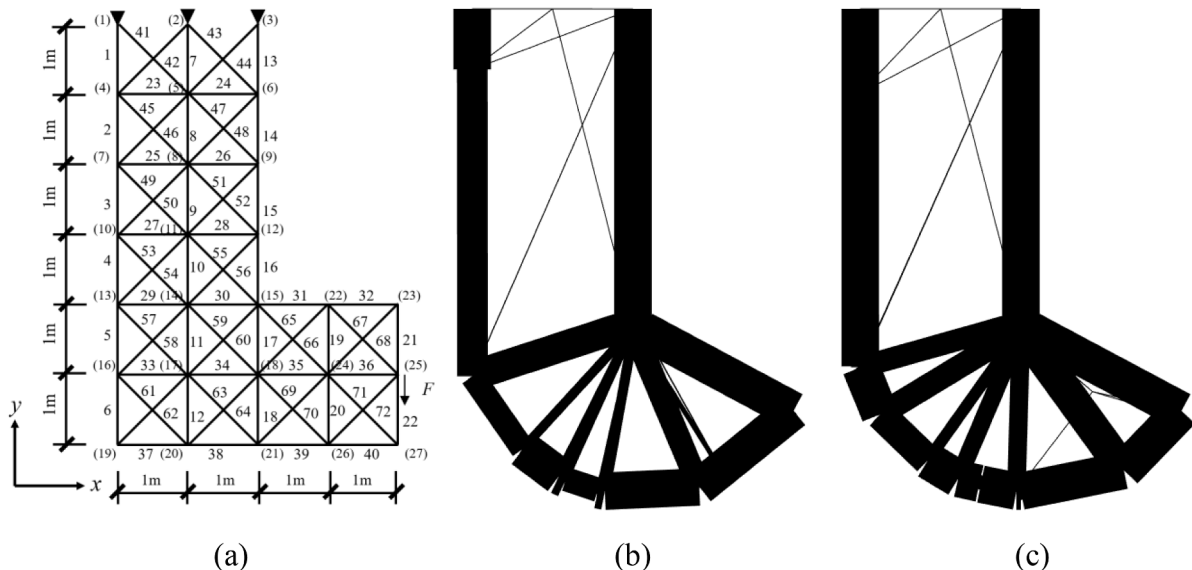


Fig. 13. Initial structure and results of example 4; (a) initial structure, (b) result at initial iteration; (c) result at final iteration.

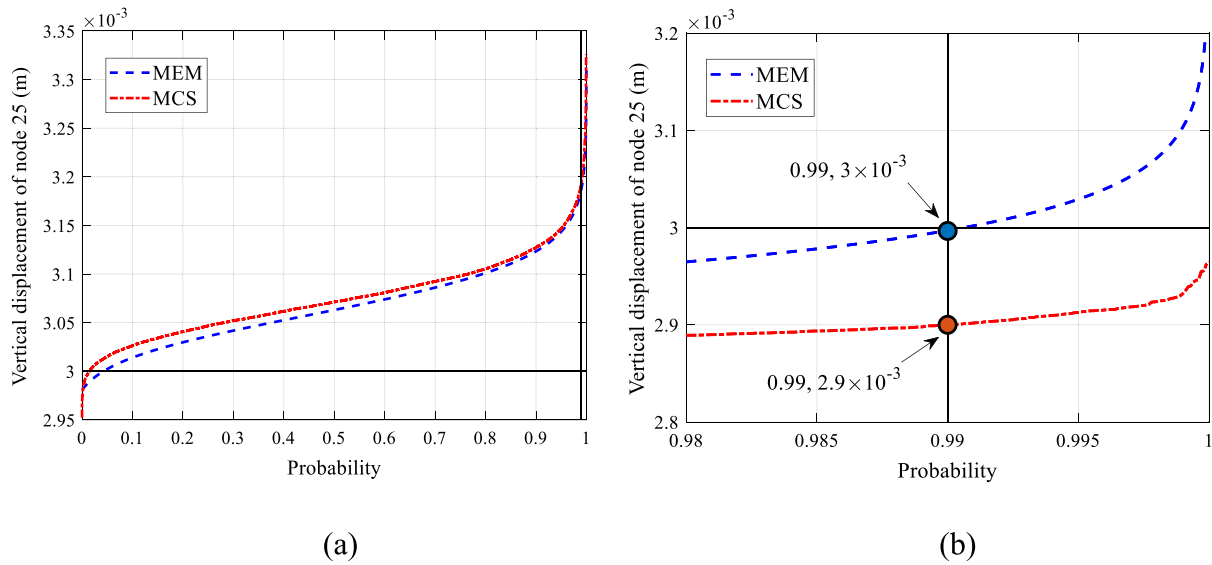


Fig. 14. Quantile functions of vertical displacement of node 25 of example 4 at the results of: (a) initial iteration; (b) final iteration.

Table 14

Location of nodes of the results of numerical example 4 at initial and final iterations.

Node	Initial iteration		Final iteration	
	x-coordinate (m)	y-coordinate (m)	x-coordinate (m)	y-coordinate (m)
1	0	6	0	6
2	1	6	1	6
3	2	6	2	6
4	0	5.2462	0	4.9501
5	2	5.9986	1.9999	5.9999
6	2	2.0829	2	2.1036
7	0.00287	1.4283	0.000913	1.5532
8	0.01077	1.4370	0.007133	1.5422
9	2	2.0283	1.9999	2.0130
10	0.6297	0.5246	0.2467	0.9546
11	0.6291	0.5290	0.2512	0.9536
12	2	2.0242	1.9999	2.0129
13	1.1939	0.1333	0.8588	0.4783
14	1.0796	0.1890	0.8413	0.3831
15	2	2	2	2
16	1.2319	0.1196	1.4423	0.0732
17	1.1663	0.1487	1.2181	0.1557
18	1.6500	0	1.9445	0
19	1.2407	0.1189	1.4847	0.0971
20	1.2395	0.1196	1.5026	0.0874
21	1.5651	0.01673	1.9999	0
22	2.8256	0.05215	2.8916	1.2369
23	3.9923	0.9971	3.8782	0.9479
24	2.0112	2	2.0186	2
25	4	1	4	1
26	3.1442	0.1853	3.2835	0.2584
27	2.1322	2	2.1240	1.9999

transformation from non-normal random space to standard normal

Appendix A.: Proof for convexity of $\Gamma(\lambda)$

Consider the following function

$$\Gamma(\lambda) = - \int_0^1 \ln \left(\sum_{r=1}^n \lambda_r K_r(u) \right) du + \sum_{r=1}^n \lambda_r h_r \quad (A1)$$

where the n variables are $\lambda = (\lambda_1, \lambda_2, \dots, \lambda_n)$; h_r and $K_r(r = 1, 2, \dots, n)$ are n constants and polynomials with arbitrary orders, respectively. Obviously,

space will increase the nonlinearity in performance function.

For the other three numerical examples of shape and topology optimization of plane frames, the optimization problem is formulated to minimize the structural volume subject to single or multiple displacement constraints. The uncertainty is considered in the x - and y -coordinates of free nodes and the cross-sectional area and Young's modulus of each member, and the result satisfying the reliability constraint can be found by the proposed method. It is demonstrated in numerical example 3 that although the reliability constraints are all satisfied after the second iteration, the result is too reliable due to the large shifting value on the upper bounds of response. By contrast, for the result at the final iteration, one of the reliability constraints is satisfied with equality and the others with inequality and the structural volume is further reduced, indicating the effectiveness of the stopping criteria to prevent obtaining a conservative result. Moreover, in the example of L-shape frame structure, the quantile function of the constraint can be also appropriately estimated by the proposed MEM with small sample size, while the total number of uncertainties has been significantly increased, indicating that the proposed method has the potential to deal with a high dimensional RBDO problem.

Declaration of Competing Interest

The authors declare that there is no conflict of interest, and they have no known competing financial interests or personal relationships that could have appeared to influence the work reported in this paper.

Acknowledgement

This research is partially supported by China Scholarship Council (File No. 201806050114).

the part $\sum_{r=1}^n \lambda_r h_r$ is convex since it is a linear combination of variables, and the other part $-\int_0^1 \ln(\sum_{r=1}^n \lambda_r K_r(u)) du$ is also convex which can be proven by using the following two operations [58].

Operation 1: Suppose $f(\lambda, u)$ is convex in λ for each $u \in \Omega$, and $\omega(u) \geq 0$ for each $u \in \Omega$, then the function g defined as

$$g(\lambda) = \int_{\Omega} \omega(u) f(\lambda, u) du \quad (\text{A2})$$

is convex in λ .

Operation 2: Suppose $f: R^n \rightarrow R$, $A \in R^{n \times m}$, and $b \in R^n$. Define $g: R^m \rightarrow R$ by

$$g(\lambda) = f(A\lambda + b) \quad (\text{A3})$$

with domain $g = \{\lambda | A\lambda + b \in \text{domain } f\}$. Then if f is convex, so is g ; if f is concave, so is g .

Because the negative logarithmic function is convex, $-\ln(\sum_{r=1}^n \lambda_r K_r(u))$ is convex for a specific value of u according to operation 2, and the integration $-\int_0^1 \ln(\sum_{r=1}^n \lambda_r K_r(u)) du$ to u is also convex according to operation 1 as $\omega(u) = 1$ for $u \in [0, 1]$. Thus, Eq. (A1) is convex.

Appendix B: Expressions of first four sample L-moments

Let X_1, X_2, \dots, X_m be the m samples of random variable X and $X_{1:m} \leq X_{2:m} \leq \dots \leq X_{m:m}$ be the corresponding order statistics. The first four sample L-moments of X , denoted as l_1, l_2, l_3 and l_4 , respectively, can be calculated as

$$l_1 = \frac{1}{m} \sum_{i=1}^m X_{i:m} \quad (\text{B-1})$$

$$l_2 = \frac{1}{m} \left(2 \sum_{i=1}^m \frac{i-1}{m-1} X_{i:m} - \sum_{i=1}^m X_{i:m} \right) \quad (\text{B-2})$$

$$l_3 = \frac{1}{m} \left(6 \sum_{i=1}^m \frac{(i-1)(i-2)}{(m-1)(m-2)} X_{i:m} - 6 \sum_{i=1}^m \frac{i-1}{m-1} X_{i:m} + \sum_{i=1}^m X_{i:m} \right) \quad (\text{B-3})$$

$$l_4 = \frac{1}{m} \left(20 \sum_{i=1}^m \frac{(i-1)(i-2)(i-3)}{(m-1)(m-2)(m-3)} X_{i:m} - 30 \sum_{i=1}^m \frac{(i-1)(i-2)}{(m-1)(m-2)} X_{i:m} + 12 \sum_{i=1}^m \frac{i-1}{m-1} X_{i:m} - \sum_{i=1}^m X_{i:m} \right) \quad (\text{B-4})$$

References

- [1] Schuëller GI, Jensen HA. Computational methods in optimization considering uncertainties - An overview. *Comput Methods Appl Mech Eng* 2008;198(1):2–13. <https://doi.org/10.1016/j.cma.2008.05.004>.
- [2] Ben-Tal A, Laurent El Ghaoui, Nemirovski A. *Robust Optimization*. Princeton University Press; 2009.
- [3] Elishakoff I, Ohsaki M. *Optimization and anti-optimization of structures under uncertainty*. London: World Scientific; 2010.
- [4] Frangopol DM. Structural optimization using reliability concepts. *J Struct Eng* 1985;111(11):2288–301. [https://doi.org/10.1061/\(ASCE\)0733-9445\(1985\)111:11\(2288\)](https://doi.org/10.1061/(ASCE)0733-9445(1985)111:11(2288)).
- [5] Choi S-K, Grandhi RV, Canfield RA. *Reliability-based structural design*. London: Springer; 2007.
- [6] Valdebenito MA, Schuëller GI. A survey on approaches for reliability-based optimization. *Struct Multidiscip Optim* 2010;42(5):645–63. <https://doi.org/10.1007/s00158-010-0518-6>.
- [7] Aoues Y, Chateauneuf A. Benchmark study of numerical methods for reliability-based design optimization. *Struct Multidiscip Optim* 2010;41(2):277–94. <https://doi.org/10.1007/s00158-009-0412-2>.
- [8] Chen X, Hasselman TK, Neill DJ. Reliability based structural design optimization for practical application. 38th AIAA/ASME/ASCE/AHS/ASC Struct. Struct. Dyn. Mater. Conf. Exh. AIAA/ASME/AHS Adapt. Struct. Forum, Kissimmee, Florida: 1997, p. 1407. doi:doi:10.2514/6.1997-1403.
- [9] Kuschel N, Rackwitz R. Two basic problems in reliability-based structural optimization. *Math Methods Oper Res* 1997;46(3):309–33. <https://doi.org/10.1007/BF01194859>.
- [10] Liang J, Mourelatos ZP, Tu J. A single-loop method for reliability-based design optimisation. *Int J Prod Dev* 2008;5:76–92. <https://doi.org/10.1504/IJPD.2008.016371>.
- [11] Enevoldsen I, Sørensen JD. Reliability-based optimization in structural engineering. *Struct Saf* 1994;15(3):169–96.
- [12] Wu Y-T. Computational methods for efficient structural reliability and reliability sensitivity analysis. *AIAA J* 1994;32(8):1717–23. <https://doi.org/10.2514/3.12164>.
- [13] Tu J, Choi KK, Park YH. A new study on reliability-based design optimization. *J Mech Des* 1999;121:557. <https://doi.org/10.1115/1.2829499>.
- [14] Lee I, Choi KK, Du L, Gorsich D. Inverse analysis method using MPP-based dimension reduction for reliability-based design optimization of nonlinear and multi-dimensional systems. *Comput Methods Appl Mech Eng* 2008;198(1):14–27. <https://doi.org/10.1016/j.cma.2008.03.004>.
- [15] Rahman S, Wei D. Design sensitivity and reliability-based structural optimization by univariate decomposition. *Struct Multidiscip Optim* 2008;35(3):245–61. <https://doi.org/10.1007/s00158-007-0133-3>.
- [16] Meng Z, Keshtegar B. Adaptive conjugate single-loop method for efficient reliability-based design and topology optimization. *Comput Methods Appl Mech Eng* 2019;344:95–119. <https://doi.org/10.1016/j.cma.2018.10.009>.
- [17] Weiji Li, Li Y. An effective optimization procedure based on structural reliability. *Comput Struct* 1994;52(5):1061–7. [https://doi.org/10.1016/0045-7949\(94\)90090-6](https://doi.org/10.1016/0045-7949(94)90090-6).
- [18] Du X, Chen W. Sequential optimization and reliability assessment method for efficient probabilistic design. *J Mech Des* 2004;126:225. <https://doi.org/10.1115/1.1649968>.
- [19] Du X. Saddlepoint approximation for sequential optimization and reliability analysis. *J Mech Des* 2008;130:1–11. <https://doi.org/10.1115/1.2717225>.
- [20] Chen Z, Qiu H, Gao L, Li P. An optimal shifting vector approach for efficient probabilistic design. *Struct Multidiscip Optim* 2013;47(6):905–20. <https://doi.org/10.1007/s00158-012-0873-6>.
- [21] Hao P, Wang Y. A new reliability-based design optimization method with multiple-design points using the active learning kriging. *Asian Congr. Struct. Multidiscip. Optim.* 2020, Seoul, Korea (Online Conference); 2020.
- [22] Li G, Yang H, Zhao G. A new efficient decoupled reliability-based design optimization method with quantiles. *Struct Multidiscip Optim* 2020;61(2):635–47. <https://doi.org/10.1007/s00158-019-02384-7>.
- [23] He W, Yang H, Zhao G, Zeng Y, Li G. A quantile-based SORA method using maximum entropy method with fractional moments. *J Mech Des* 2021;143:1–12. <https://doi.org/10.1115/1.4047911>.
- [24] Li G, He W, Zeng Y. An improved maximum entropy method via fractional moments with Laplace transform for reliability analysis. *Struct Multidiscip Optim* 2019;59(4):1301–20. <https://doi.org/10.1007/s00158-018-2129-6>.
- [25] Do B, Ohsaki M, Yamakawa M. Sequential mixture of Gaussian processes and saddlepoint approximation for reliability-based design optimization of structures. *Struct Multidiscip Optim* 2021;64(2):625–48.
- [26] Kanno Y. A data-driven approach to non-parametric reliability-based design optimization of structures with uncertain load. *Struct Multidiscip Optim* 2019;60(1):83–97. <https://doi.org/10.1007/s00158-019-02199-6>.
- [27] Yamakawa M, Ohsaki M. Fail-safe topology optimization via order statistics with stochastic gradient descent. *Asian Congr. Struct. Multidiscip. Optim.* 2020, Seoul, Korea (Online Conference); 2020.

- [28] Hosking JRM. L-Moments: Analysis and estimation of distributions using linear combinations of order statistics. *J R Stat Soc Ser B* 1990;52(1):105–24. <https://doi.org/10.1111/rssb.1990.52.issue-110.1111/j.2517-6161.1990.tb01775.x>.
- [29] Zhao Y-G, Tong M-N, Lu Z-H, Xu J. Monotonic expression of polynomial normal transformation based on the first four L-moments. *J Eng Mech* 2020;146(7): 06020003. [https://doi.org/10.1061/\(ASCE\)JEM.1943-7889.0001787](https://doi.org/10.1061/(ASCE)JEM.1943-7889.0001787).
- [30] Lee U, Lee I. Sampling-based reliability analysis using deep feedforward neural network. *Asian Congr. Struct. Multidiscip. Optim.* 2020, Seoul, Korea (Online Conference): n.d.
- [31] Vapnik VN. *The nature of statistical learning theory*. Springer Science & Business Media; 2013.
- [32] Pandey MD. A direct approach to the estimation of quantile function using the maximum entropy principle. *Struct Saf* 2000;22:4.
- [33] Deng J, Pandey MD. Estimation of the maximum entropy quantile function using fractional probability weighted moments. *Struct Saf* 2008;30(4):307–19. <https://doi.org/10.1016/j.strusafe.2007.05.005>.
- [34] Pandey MD. Extreme quantile estimation using order statistics with minimum cross-entropy principle. *Probabilistic Eng Mech* 2001;16(1):31–42. [https://doi.org/10.1016/S0266-8920\(00\)00004-7](https://doi.org/10.1016/S0266-8920(00)00004-7).
- [35] Pandey MD. Minimum cross-entropy method for extreme value estimation using peaks-over-threshold data. *Struct Saf* 2001;23(4):345–63. [https://doi.org/10.1016/S0167-4730\(02\)00008-5](https://doi.org/10.1016/S0167-4730(02)00008-5).
- [36] Hosking JRM. Distributions with maximum entropy subject to constraints on their L-moments or expected order statistics. *J Stat Plan Inference* 2007;137(9): 2870–91. <https://doi.org/10.1016/j.jspi.2006.10.010>.
- [37] Bendsoe MP, Ben-Tal A, Zowe J. Optimization methods for truss geometry and topology design. *Structural Optim* 1994;7:141–59. <https://doi.org/10.1117/12.660870>.
- [38] Stolpe M. Truss optimization with discrete design variables: a critical review. *Struct Multidiscip Optim* 2016;53(2):349–74. <https://doi.org/10.1007/s00158-015-1333-x>.
- [39] Bendsoe MP, Sigmund O. *Topology Optimization: Theory, Methods, and Applications*. Springer; 2003. doi:10.1063/1.3278595.
- [40] Ohsaki M. *Optimization of finite dimensional structures*. Boca Raton: CRC Press; 2010.
- [41] Zegard T, Paulino GH. GRAND3 — Ground structure based topology optimization for arbitrary 3D domains using MATLAB. *Struct Multidiscip Optim* 2015;52(6): 1161–84. <https://doi.org/10.1007/s00158-015-1284-2>.
- [42] Sokół T. A 99 line code for discretized Michell truss optimization written in Mathematica. *Struct Multidiscip Optim* 2011;43(2):181–90. <https://doi.org/10.1007/s00158-010-0557-z>.
- [43] Gil L, Andreu A. Shape and cross-section optimization of a truss structure. *Comput Struct* 2001;79:681–9. [https://doi.org/10.1016/S0045-7949\(00\)00182-6](https://doi.org/10.1016/S0045-7949(00)00182-6).
- [44] Wang D, Zhang WH, Jiang JS. Truss shape optimization with multiple displacement constraints. *Comput Methods Appl Mech Eng* 2002;191(33): 3597–612. [https://doi.org/10.1016/S0045-7825\(02\)00297-9](https://doi.org/10.1016/S0045-7825(02)00297-9).
- [45] Achtziger W. On simultaneous optimization of truss geometry and topology. *Struct Multidiscip Optim* 2007;33(4-5):285–304. <https://doi.org/10.1007/s00158-006-0092-0>.
- [46] Ohsaki M. Simultaneous optimization of topology and geometry of a regular plane truss. *Comput Struct* 1998;66(1):69–77. [https://doi.org/10.1016/S0045-7949\(97\)00050-3](https://doi.org/10.1016/S0045-7949(97)00050-3).
- [47] Ohsaki M, Hayashi K. Force density method for simultaneous optimization of geometry and topology of trusses. *Struct Multidiscip Optim* 2017;56(5):1157–68. <https://doi.org/10.1007/s00158-017-1710-8>.
- [48] Hayashi K, Ohsaki M. FDMopt: Force density method for optimal geometry and topology of trusses. *Adv Eng Softw* 2019;133:12–9. <https://doi.org/10.1016/j.advengsoft.2019.04.002>.
- [49] Shen W, Ohsaki M. Geometry and topology optimization of plane frames for compliance minimization using force density method for geometry model. *Eng Comput* 2021;37(3):2029–46. <https://doi.org/10.1007/s00366-019-00923-w>.
- [50] Moustapha M, Sudret B, Bourinet J-M, Guillaume B. Quantile-based optimization under uncertainties using adaptive Kriging surrogate models. *Struct Multidiscip Optim* 2016;54(6):1403–21. <https://doi.org/10.1007/s00158-016-1504-4>.
- [51] Melchers RE, Beck AT. *Structural Reliability Analysis and Prediction*. John Wiley & sons; 2018.
- [52] Der Kiureghian A, Liu P-L. Structural reliability under incomplete probability information. *J Eng Mech* 1986;112(1):85–104.
- [53] Tong M-N, Zhao Y-G, Lu Z-H. Normal transformation for correlated random variables based on L-moments and its application in reliability engineering. *Reliab Eng Syst Saf* 2021;207:107334. <https://doi.org/10.1016/j.res.2020.107334>.
- [54] Hosking J, Wallis JR. *Regional frequency analysis: an approach based on L-moments*. Cambridge University Press; 2005.
- [55] Xi Z, Hu C, Youn BD. A comparative study of probability estimation methods for reliability analysis. *Struct Multidiscip Optim* 2012;45(1):33–52. <https://doi.org/10.1007/s00158-011-0656-5>.
- [56] Mathworks. *Optimization Toolbox User's Guide R2018a*. 2018.
- [57] Ulaganathan S, Couckuyt I, Dhaene T, Degroote J, Laermans E. High dimensional Kriging metamodeling utilising gradient information. *Appl Math Model* 2016;40 (9-10):5256–70. <https://doi.org/10.1016/j.apm.2015.12.033>.
- [58] Boyd S, Vandenberghe L. *Convex Optimization*. Cambridge University Press; 2004. doi:10.1109/TAC.2006.884922.